Digitized Theses

Digitized Special Collections

2007

Microstructural Effects on the Nanoindentation Creep of a 2024 Aluminum Alloy at 300K

Bipasha Bose
Western University

Follow this and additional works at: https://ir.lib.uwo.ca/digitizedtheses

Microstructural Effects on the Nanoindentation Creep of a 2024 Aluminum
Alloy at 300K

(Spine title: Nanoindentation Creep of the 2024 Al Alloy)

(Thesis format: Integrated-Article)

by

Bipasha <u>Bose</u>

Graduate Program in Engineering Science

Department of Mechanical and Materials Engineering

A thesis submitted in partial fulfillment

of the requirements for the degree of

Master of Engineering Science

Faculty of Graduate Studies

The University *of* Western Ontario

London, Ontario, Canada

August 2007

ABSTRACT

Constant force nanoindentation creep tests were performed on 2024 aluminum to assess the dependence of the indentation creep rate upon indentation depth h, crystal orientation, distance L to a grain boundary and grain boundary misorientation angle θ. The initial and final indentation stress ($\sigma_{ind(t=0)}$ and σ_{th}), the apparent activation energy and volume (ΔG_0 and V^*) were calculated. $\sigma_{ind(t=0)}$ and σ_{th} were dependent upon h while ΔG_0 was not. V^* followed the same dependence upon dislocation density and indentation stress regardless of h indicating that the basic dislocation/obstacle interaction controlling the indentation creep rate is independent of h. Tests performed directly upon grain boundaries of known θ indicated that $\sigma_{ind(t=0)}$, σ_{th}, and ΔG_0 of the boundaries could be expressed in the same functional form as the Read-Shockley equation for the energy of small angle boundaries. A modified Hall-Petch type equation was developed to express $\sigma_{ind(t=0)}$, σ_{th}, and ΔG_0 in terms of θ and L.

Keywords: Nanoindentation, creep, aluminum, heat treatment, grain size, misorientation angle, crystal orientation

CO-AUTHORSHIP

The research presented in this thesis is composed of two manuscripts co-authored by Bipasha Bose and Dr. Robert J. Klassen. The first part of the research materials was submitted to Journal of Materials Science and is presently under review. The second part is in the process of being submitted.

The experiments, data analysis and manuscript drafting were performed by Bipasha Bose. Suggestions for the interpretation of the data and the editing of the manuscript were carried out by Dr. Robert J. Klassen.

Dedications

To My Beloved Parents & Husband, Mrinmoy Kanungo

ACKNOWLEDGEMENT

The work presented in this thesis would not have been possible without the help and cooperation of the people I would like to acknowledge here.

I would start by expressing my deep gratitude to my supervisor Professor Robert J. Klassen for his continuous guidance and immense support throughout my graduate studies at Western. Without him, it would have been impossible for me to accomplish the work I have done so far.

I would also like to thank Professor B.J. Diak and Atish K. Ray of Queen's University for their selfless help and effort regarding the EBSD experiments.

Special notes of thanks are due to Mr. Bert Verhagen from the Department of Mechanical and Materials Engineering and Dr. Dmitrij Zagidulin, Dr. Jamie J. Noel from the Department of Chemistry for their technical guidance in using all the equipment in their respective labs.

My heartiest gratitude goes to my colleague, Vineet Bhakhri for his selfless help and encouragement throughout this endeavor.

Last but not the least, I wish to thank the Natural Science and Engineering Research Council of Canada who provided financial support for this research through the Discovery Grant program.

TABLE OF CONTENTS

CHAPTER 5 – EFFECT OF CRYSTAL ORIENTATION AND GRAIN BOUNDARIES ON THE NANOINDENTATION CREEP OF A 2024 ALUMINUM ALLOY AT 300K

CHAPTER 6 – CONCLUSIONS AND RECOMMENDATIONS FOR FUTURE WORK

LIST OF FIGURES

creep tests respectively. They are therefore analysed for their dependence upon indentation depth in Fig. 4.6.

4.6 Variation in: **(a)** $\sigma_{ind(t=0)}$ with initial indentation depth, h_0 and **(b)** σ_{th} with final indentation depth, h_f for the 2024 aluminum alloy in the As-Quenched (AQ), Peak-Aged (PA) and Over-Aged (OA) conditions. $\sigma_{ind(t=0)}$ and σ_{th} both decrease with increasing indentation depth although $\sigma_{ind(t=0)}$ shows a stronger dependence upon indentation depth than does σ_{th}. The trend displayed by $\sigma_{ind(t=0)}$ is similar to that previously reported for the dependence of the indentation hardness of naturally aged 2024 aluminum alloy upon indentation depth [12]. The power-law functions fitted to the data in Fig. 4.6(b) indicate that σ_{th} is sensitive to heat treatment. σ_{th} is largest, for a given indentation depth, for the peak-aged condition followed by the as-quenched and finally the over-aged conditions.

4.7 Thermal activation energy, $\Delta G(\tau_{eff})$, normalized with respect to μb^3, versus the effective indentation shear stress, τ_{eff} for all indentation tests performed on the peak-aged 2024 aluminum alloy. Similar results were obtained for the over-aged and as-quenched conditions indicating that while $\Delta G(\tau_{eff})$ increases with decreasing τ_{eff} it is essentially independent of heat-treatment and indentation depth. Labelled on the plot is the apparent total activation energy ΔG_0 determined by extrapolating $\Delta G(\tau_{eff})$ to $\tau_{eff} = 0$.

4.8 Average activation energy, $\Delta G_0/\mu b^3$ versus final indentation depth, h_f for As Quenched (AQ), Peak-Aged (PA) and Over-Aged (OA) samples of the 2024 aluminum alloy tested in this study and for polycrystalline gold [7]. The magnitude of ΔG_0 for the 2024 aluminum alloy ranges from 0.17 to 0.2 μb^3. ΔG_0 is larger for the 2024 aluminum alloy than for the gold indicating the effect of alloy additions on the activation energy

LIST OF TABLES

Chapter 1

Introduction

Constant load microindentation creep tests have been a focal point of researchers for over a decade [1-7]. It has been observed that the time-dependent plastic deformation that occurs during these tests occurs by a deformation mechanism involving obstacle-limited dislocation glide. In most cases, the investigations were carried out on pure metals with the effect of second phase particles being often ignored. It is the objective of this thesis, therefore, to investigate the effect of second phase particles on the time-dependent plastic deformation of a metal alloy during nanoindentation at room temperature. During the investigation, grain-to-grain variations of the deformation parameters were also observed. This provided the second objective of this study; namely to investigate the effect of grain boundaries and grain orientation on the deformation process during nanoindentation creep tests. Therefore, the ultimate objective of this thesis is to study the effect of heat-treatment, grain boundaries and grain orientation on the nanoindentation creep of an Aluminum 2024 alloy during nanoindentation.

Chapter 2 of this thesis contains a review of relevant published literature related to the theory of deformation mechanisms, the effect of grain size on the plastic deformation of metals, the basic theory of Electron Back Scattered Diffraction (EBSD), the process of crystal orientation measurement and finally the various microstructural features that can be created in an 2024 aluminum alloy by heat-treatment. Chapter 3 provides a description of the instrumented nanoindentation test and the testing equipment used for the experiments described in the subsequent chapters.

The investigations related to the first part of our objective, that is the effect of the second phase particles on nanoindentation creep of an aluminum alloy under different thermal conditions is presented in Chapter 4. In this Chapter, the deformation parameters, such as thermal activation energy, inter-obstacle spacing and threshold indentation stress are

calculated from the experimental data and compared to assess the differences that occur in a 2024 aluminum alloy subjected to different heat treatments.

Chapter 5 presents the research carried out to address the second objective of the thesis; namely to study the effect of grain boundaries and crystal orientation on the deformation parameters of the 2024 aluminum alloy.

A slightly modified version of Chapter 4 has been submitted to the Journal of Materials Science (April 2007) and is currently being reviewed. A version of Chapter 5 is in the process of being prepared for journal submission.

Chapter 6 presents the general conclusions that can be drawn from the experimental results and analyses presented in Chapters 4 and 5.

References:

[1] Li W. B., Henshall J. L., Hooper R. M., Easterling K. E., *Acta metal. Mater.* v.39 (1991), p. 3099

[2] Sargent P. M., Ashby M. F., *Mater. Sci. Tech.*, v. 8 (1992), p. 594.

[3] Takagi H., Dao M., Fujiwara M., Otsuka M. *Philos. Mag.* v. 83 (2003), p. 3959

[4] Newson W. R., Diak B. J., Saimoto S., *Thin Films: Stresses and Mechanical Properties VI*, v. 436 (1997), p. 359, MRS Publications, Warrendale, PA, USA

[5] Bhakhri V., Klassen R. J., *J. Mater. Sci.*, v. 41 (2006), p. 2259

[6] Bhakhri V., Klassen R. J., *J. Mater. Sci.*, v. 41 (2006), p. 2249

[7] Bhakhri V., Klassen R. J., *Scripta Mater.*, v. 55 (2006), p. 395

Chapter 2
Literature Review

The objective of this thesis is to study the effect of second phase particles, grain size and orientation on the time dependent plastic deformation of a heat-treatable aluminum alloy. This chapter presents a review of the published literature that is relevant to this objective. The chapter includes a description of the mechanism of time dependent plastic deformation in metals and the rate equations that describe these mechanisms. Sections 2.2 and 2.3 present theories on the grain size and grain boundary misorientation on the local plastic deformation of polycrystalline metals. The basics of EBSD and crystallographic orientation measurements are described in Section 2.4. Section 2.5 gives a short description of the different steps of the heat-treatment process of an Al-4%Cu alloy (the 2024 alloy studied in this thesis). The structures formed during the heat-treatment process and the relationships of these structures to the indentation hardness of the alloy are described in Sections 2.6 and 2.7 respectively.

2.1 Deformation Mechanisms and Rate Equations

A general description of the theories used to predict the rate of time-dependent plastic deformation of ductile metals, such as Aluminum, is discussed in this section.

Among various deformation mechanisms, the one that will contribute the most to the total rate of deformation depends on the stress, temperature and properties of the solid. For a particular material, a diagram called deformation mechanism map can represent the field of dominance of each deformation mechanism. Figure 2.1 is a deformation mechanism map for pure aluminum showing the fields of different dominating mechanisms based on stress and temperature. As the experiments performed in this thesis were carried out at room temperature (27°C), the constant-load pyramidal indentation creep can be expressed in terms of a deformation process involving the mechanism of low temperature obstacle-

limited dislocation glide (L.T. Creep region in Figure 2.1). This mechanism is described in Section 2.1.1.
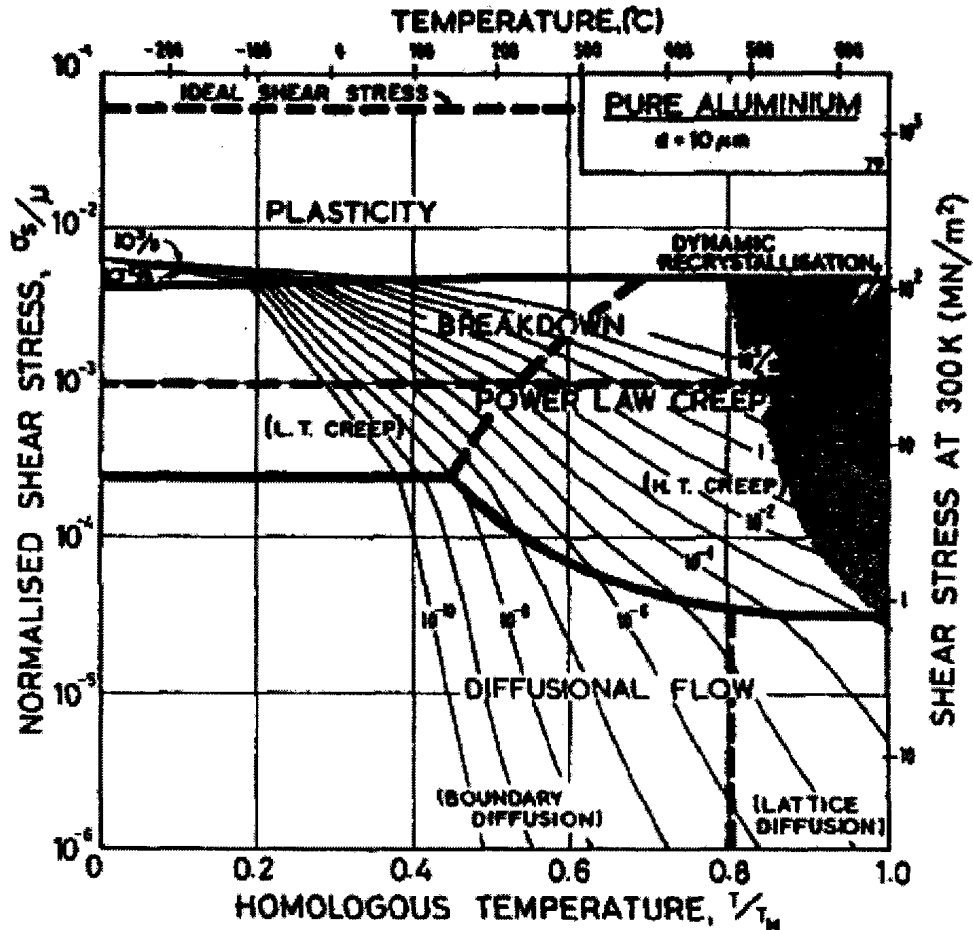
Figure 2.1: Deformation mechanism map for pure aluminum having grain size of 10 μm [4]. The plastic deformation occurring in the region identified as ''L. T. Creep'' occurs by obstacle limited dislocation glide. It is within this region that indentation creep tests performed at room temperature occur.

2.1.1 Low-Temperature ($T<0.3T_{melt}$) Plasticity by Obstacle Limited Dislocation Glide

At absolute temperatures less than about $0.3T_{melt}$ the rate of movement of dislocations within a metal crystal is no longer directly dependent upon the rate of solid-state

diffusion; rather it is controlled by the rate at which a dislocation can move past a discrete obstacle solely by having sufficient thermal vibrational energy at the dislocation/obstacle interface.

The motion of dislocations is always obstacle limited. These obstacles may be other dislocations, solute atoms, second phase precipitates, grain boundaries, or the lattice itself (i.e. Peierl's stress). When mobile dislocations, having a population (i.e. dislocation density) ρ_m move through a field of obstacles with an average velocity $\bar{v}$, they produce a shear strain rate in the crystal of:

$$\dot{\gamma} = \rho_m \, b \, \bar{v} \tag{2.1}$$

Where, b is the magnitude of the Burger's vector of the dislocation. The velocity $\bar{v}$ is almost entirely determined by the waiting time of the dislocations at the obstacles.

At steady state, ρ_m is a function of stress and temperature only and can be expressed as

$$\rho_m = \alpha \left(\frac{\tau}{\mu(T)b} \right)^2 \tag{2.2}$$

Where, τ is shear stress, α is a constant of order unity and $\mu(T)$ is the temperature dependent elastic shear modulus of the material [1].

Let us consider a dislocation of length ℓ, gliding under an applied force $\tau b \ell$ in the direction x. If the dislocation encounters obstacles each of which is capable of producing a resisting force F that is larger than $\tau b \ell$, the dislocation will stop at a position x_1, as shown schematically in Figure 2.2.

To move towards a position x_2 the dislocation will have to overcome the obstacle. The total area beneath the force versus distance curve illustrated in Figure 2.2 is the total

energy (ΔG_0) required for a dislocation to move past the obstacle. Part of this energy comes from mechanical work done by the applied force and can be expressed as τV^*, where, $V^* = b\ell(x_2-x_1)$ is the activation volume. The mechanical contribution, τV^*, is not large enough to push the dislocation past the obstacle. So, the remainder of the energy must be provided by thermal fluctuations of the atoms in the immediate vicinity of the dislocation/obstacle interface. The thermal energy $\Delta G(\tau)$ which must be supplied can be expressed as,

$$\Delta G(\tau) = \Delta G_0 - \tau V^*$$

(2.3)
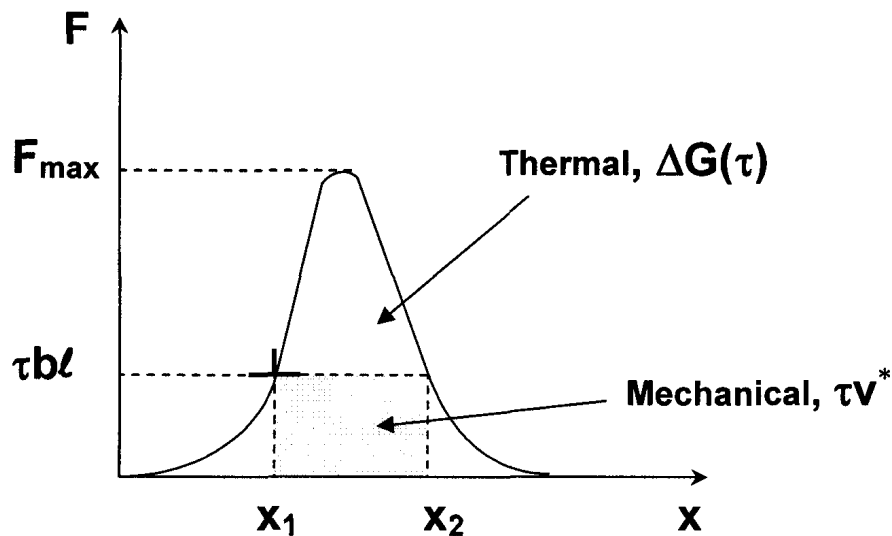
Figure 2.2: Profile of resistance force (F) versus distance (x) for barriers opposing dislocation motion.

The probability of thermal vibrations producing the thermal activation energy $\Delta G(\tau)$ at temperature T is represented by the Boltzmann factor $exp(-\Delta G(\tau)/kT)$ [2]. So, the velocity of the dislocations, effectively vibrating at a frequency v, and having a thermal activation energy $\Delta G(\tau)$ can be expressed by the kinetic equation,

$$\bar{v} = \beta b v \, exp - \frac{\Delta G(\tau)}{kT}$$

(2.4)

Where, β is a dimensional constant, b is the magnitude of Burger's vector and v is the frequency of atomic vibration at 0°K (Debye frequency with a value of $10^{12}s^{-1}$).

Considering all shapes and distribution of obstacles, Kocks et al. [3] proposed the following general equation which shows the dependence of $\Delta G(\tau)$ upon τ

$$\Delta G(\tau) = \Delta G_0 \left[1 - \left(\frac{\tau}{\hat{\tau}} \right)^p \right]^q$$ (2.5)

Where, $\hat{\tau}$ is the "athermal" flow strength of the material at 0°K. p,q are the constants that define the shape of the force/distance curve for the obstacle. Their values are usually bounded by $0 \le p \le 1$, $1 \le q \le 2$.

The thermal activation energy, ΔG_0, characterizes the strength of a single obstacle. The classification of obstacles by their strength is given in the Table 2.1.

Obstacle strength	ΔG_0	Examples
Strong	$2 \mu b^3$	Dispersions: large or strong precipitates
Medium	$0.2\text{-}1.0 \mu b^3$	Forest dislocations, small or weak precipitates
Weak	$<0.2 \mu b^3$	Lattice resistance; solution hardening

Table 2.1: Classification of obstacles according to their strength [4]

Substituting Equations (2.2), (2.4) and (2.5) into Equation (2.1) we obtain the rate equation for discrete-obstacle controlled plasticity [4]:

$$\dot{\gamma} = \dot{\gamma}_0 \, \exp\left\{-\frac{\Delta G_0}{kT}\left(1-\left(\frac{\tau}{\hat{\tau}}\right)^p\right)^q\right\}$$ (2.6)

Where,

$$\dot{\gamma}_0 = \frac{\alpha}{b}\left(\frac{\tau}{\mu}\right)^2 \beta \, b \nu$$ (2.7)

Here, μ is the elastic shear modulus, k is Boltzmann's constant ($= 1.38 \times 10^{23}$ J/K). When ΔG_0 is large, $0.2 < \Delta G_0/\mu b^3 < 2$, the stress dependence of the exponential term is so large that that of the pre-exponential term in Equation 2.6 can be ignored. Then $\dot{\gamma}_0$ can be treated as a constant ($\dot{\gamma}_0 = 10^6$ /s). [4]

The velocity of a dislocation in most polycrystalline solids is also limited by its interaction with the atomic structure itself. This is called Peierls force or lattice resistance. The crystal lattice presents an array of long, straight barriers to the moving dislocation. With the help from the applied stress and thermal energy the dislocation advances by throwing forward kink pairs which subsequently spread apart [4,5].

The dislocation velocity is limited by the nucleation rate of kink-pairs. In this mechanism the Gibbs free energy of activation depends on the dislocation energy fluctuations with distance, and on the applied stress and temperature.

For all reasonable shapes of lattice resistance form a family the activation energies can be expressed as:

$$\Delta G(\tau) = \Delta F_p\left[1-\left(\frac{\tau}{\hat{\tau}}\right)^p\right]^q$$ (2.8)

Where, ΔF_p is the Helmholtz free energy of an isolated pair of dislocation kinks.

Substituting equations (2.1), (2.2) and (2.4) into equation (2.8) gives a model-based rate equation for plasticity limited by a lattice resistance:

$$\dot{\gamma} = \dot{\gamma}_P \left(\frac{\tau}{\mu}\right)^2 \exp\left\{ -\frac{\Delta F_p}{kT}\left[1 - \left(\frac{\tau}{\hat{\tau}_p}\right)^p\right]^q\right\}$$
(2.9)

Where, γ_p is a constant approximately equal to 10^{11} s^{-1}. For small ΔF_p, the mobile dislocation density varies with stress, and results in the pre-exponential of Equation 2.9 containing a term in τ^2.

Dislocation glide is also influenced by alloy additions. Single solute atoms in a very dilute solution, or local concentration fluctuation in a more concentrated solution, often act as stationary weak obstacles for moving dislocations. This mechanism can be expressed by the same equation to Equation 2.6 with a larger value of $\hat{\tau}$ and a smaller value of ΔG_0.

Finely dispersed precipitates can be cut through by the moving dislocations. The athermal flow strength, $\hat{\tau}$ which is inversely proportional to the particle spacing, would be large if the population of the particles is high. However the activation energy ΔG_0 is low as the flow strength for this case is strongly temperature dependent. If the precipitates are allowed to coarsen, they will behave like a dispersion of strong particles. The gliding dislocation can then only move by bowing between the obstacles or by passing them. This leads to a flow strength which has a very large activation energy, $\Delta G_0 \geq 2\mu b^3$. This flow strength is also known as the "Orowan Strengthening"[3]. To investigate these hypotheses of the effect of obstacle size on ΔG_0, different sizes and amount of second phase particles were produced by precipitation heat-treatment (Section 2.5) of a 2024 aluminum alloy at 190°C for different lengths of time (Chapter 4).

2.1.2 High Temperature Plasticity ($T > 0.3T_{melt}$) by Climb-Limited Dislocation Glide (Power-Law Creep)

The strain rate dependence of flow strength above $0.3T_{melt}$ for pure metals and above $0.4T_{melt}$ for alloys or ceramics can be expressed by an equation of the form

$$\dot{\gamma} \propto \left(\frac{\tau}{\mu}\right)^n \tag{2.10}$$

In this high temperature regime, n has a value between 3 and 10 and the resulting time-dependent deformation is referred to a power-law creep (Figure 2.1).

At high temperatures ($T > 0.6T_m$), dislocations can climb as well as glide. When the movement of a gliding dislocation is hindered by discrete obstacles, it can move past the obstacle by the mechanism of diffusion-assisted dislocation climb. This mechanism is referred as climb controlled creep. The distinguishing feature of this mechanism is the rate-controlling process, which involves diffusion of atoms, or vacancies, to or from a dislocation that is pinned by an obstacle.

The velocity υ_c at which an edge dislocation climbs over obstacles under a local normal stress σ_n acting parallel to its Burgers' vector, has been proposed by Hirth and Lothe [6] as follows:

$$\upsilon_c \approx \frac{D_\upsilon \sigma_n \Omega}{bkT} \tag{2.11}$$

Where, Ω is the atomic volume ($\approx b^3$). The lattice diffusion coefficient D_υ can be expressed as, $D_\upsilon = D_0 \, exp\left(-\frac{Q_\upsilon}{RT}\right)$, where D_0, Q_υ are material constants and R is the universal gas constant = 8.314 J/mole K

The basic climb-controlled creep equation can be obtained by making two assumptions:

1) σ_n is proportional to τ; i.e. $\sigma_n = A\tau$, where A is a material constant (of order unity)

2) $\bar{\upsilon}$ is proportional to rate at which the dislocation climbs, υ_c

The dislocation climb velocity can then be expressed as, $\quad \upsilon_c \approx \dfrac{D_\upsilon A \tau b^2}{kT}$ $\qquad$ (2.12)

Combining equations (2.1), (2.2) and (2.12), we then obtain the strain rate resulting from diffusion-limited power law creep,

$$\dot{\gamma} = \frac{A D_\upsilon \mu b}{kT} \left(\frac{\tau}{\mu}\right)^n \quad \text{, where n} \cong 3 \qquad (2.13)$$

2.1.3 High-Temperature Plasticity by Diffusional Flow

At very high temperatures, many metals display viscous creep. That is their creep rate becomes directly proportional to the applied stress and inversely proportional to the grain size.

If both lattice and grain boundary diffusion are permitted, the rate-equation for diffusional flow becomes:

$$\dot{\gamma} = \frac{42\tau\Omega}{kTd^2} D_{eff} \qquad (2.14)$$

Where the diffusion coefficient can be expressed as,

$$D_{eff} = D_\upsilon \left[1 + \frac{\pi\delta}{d}\frac{D_b}{D_\upsilon}\right]$$

Here, D_b is the grain boundary diffusion coefficient, d is the grain size and δ is the effective thickness of the boundary

At high temperatures lattice diffusion controls the rate where as at lower temperatures grain boundary diffusion takes over.

When the temperature is very high, near the melting temperature of the material, significant bulk deformation takes place by local differences in the rate of diffusion. This phenomenon is mostly seen in polycrystalline materials where large diffusive flux exists through and around, the surfaces of the grains. This flux leads to a deformation by what is known as grain boundary sliding.

2.2 Effect of grain size on the local plastic deformation

It is well known that the grain size of a polycrystalline material has an important effect on properties such as the yield stress. One of the objectives of this thesis was to measure the grain sizes of a very localized area around where the indentation creep tests are performed to observe whether the grain size and orientation, have any effect on the local indentation creep rate.

Several properties such as, yield stress, flow stress, hardness and ductility of a polycrystalline material have been reported to be dependent on the grain size of the material [7,8]. An increase in hardness and yield stress resulting from a decrease in grain size can be described by the well-established Hall-Petch relationship [9,10]:

$$\sigma = \sigma_0 + kd^{-\frac{1}{2}}$$
(2.15)

where, σ is the uniaxial yield stress of a polycrystalline material, d is the grain size and σ_0 and k are material constants. This equation is based on the concept that grain boundaries act as barriers to dislocation motion [11]. The Hall-Petch equation was further extended to relate the flow stress at a given plastic strain to the grain size of a polycrystalline material [12,13].

A similar equation can be used to relate the hardness (H) of a polycrystalline material with the grain size (d) [10]:

$$H = H_0 + k_H d^{-\frac{1}{2}} \tag{2.16}$$

where H_0 and k_H are material constants. These equations were successfully tested for wide range of polycrystalline materials. However evidence of significant deviation from these equations was observed especially for fine, ultra-fine and nano-crystalline materials [14,15]. For example, investigations showed that the strength of nano-crystalline materials (d < 15nm) is expected to decrease with further grain refinement, which is known as inverse Hall-Petch effect [16]. This thesis investigates in Chapter 5, how the parameters that describe time-dependent plastic deformation, primarily nanoindentation creep, conform to a modified Hall-Petch type of dependence upon grain proximity and angular misorientation.

2.3 Effect of grain boundary misorientation

The previous section has shown the effect of grain size on increasing the flow stress and indentation hardness of polycrystalline metals. The effect is clearly a result of the grain boundary acting as an obstacle to the gliding of dislocations through the material. It follows, therefore, that the effectiveness of a grain boundary must depend upon the particular grain boundary structure. The most fundamental parameter of the structure of a grain boundary is its angular misorientation θ (Figure 2.3 (a)).

When the angular misorientation across a grain boundary is small the boundary can be thought of as a vertical array of edge dislocations, of Burgers vector b, having a spacing $D = \frac{b}{\theta}$ (Figure 2.3(b)). The energy E of the grain boundary is then related to the elastic energy of the dislocation array.

Read and Shockley [17,18] have calculated E as a function of θ, and found that when θ is small E can be expressed as

$$E = E_0\theta\,[A - \ln\theta] \qquad\qquad (2.17)$$

where E_0 and A are material constants.
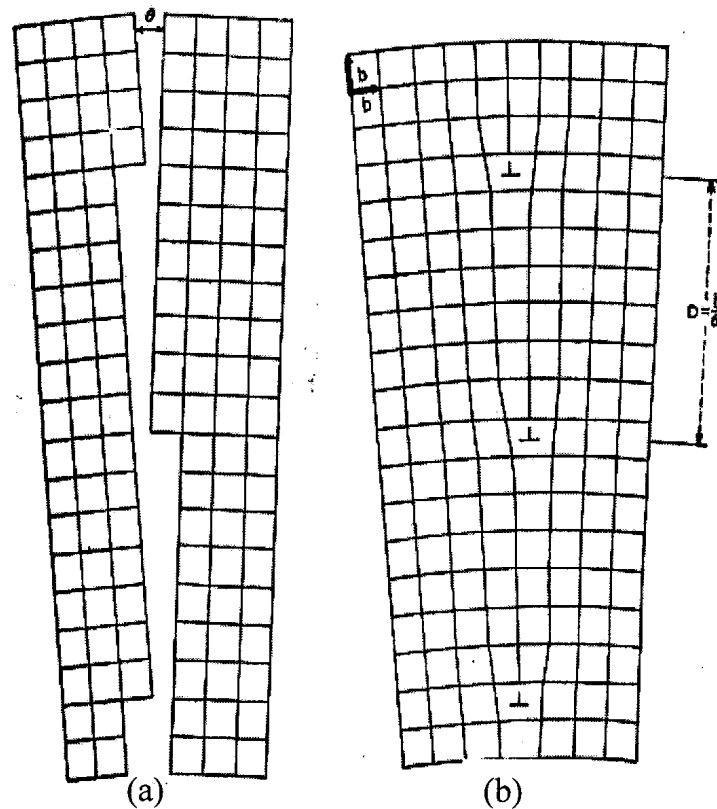
Figure 2.3: A simple grain boundary between two grains. The plane of this figure is parallel to a cube face and normal to the axis of relative rotations of the two grains. (a) Both the grains have common cube axis and the misorientation angle is θ. (b) A bicrystal formed by joining the two grains. The boundary can be thought of as a vertical array of edge dislocations ($\perp$) of Burgers vector b, having a spacing D, as the angular misorientation θ across the grain boundary is small [19].

The relative energies of grain boundaries can be measured experimentally. The most common technique is to consider the angles between three grains that meet at a single "triple point" in a material (Figure 2.4). For equilibrium to exist at the triple point the energies of the three boundaries (E_1, E_2, E_3) must be related to each other as

$$\frac{E_1}{Sin\,\psi_1} = \frac{E_2}{Sin\,\psi_2} = \frac{E_3}{Sin\,\psi_3} \tag{2.18}$$

where ψ_i are the angles between the boundaries (Figure 2.4). The crystallographic orientation of each grain can be determined by X-ray diffraction and, thus, the angle θ of each grain boundary can be calculated (See section 2.4.2).
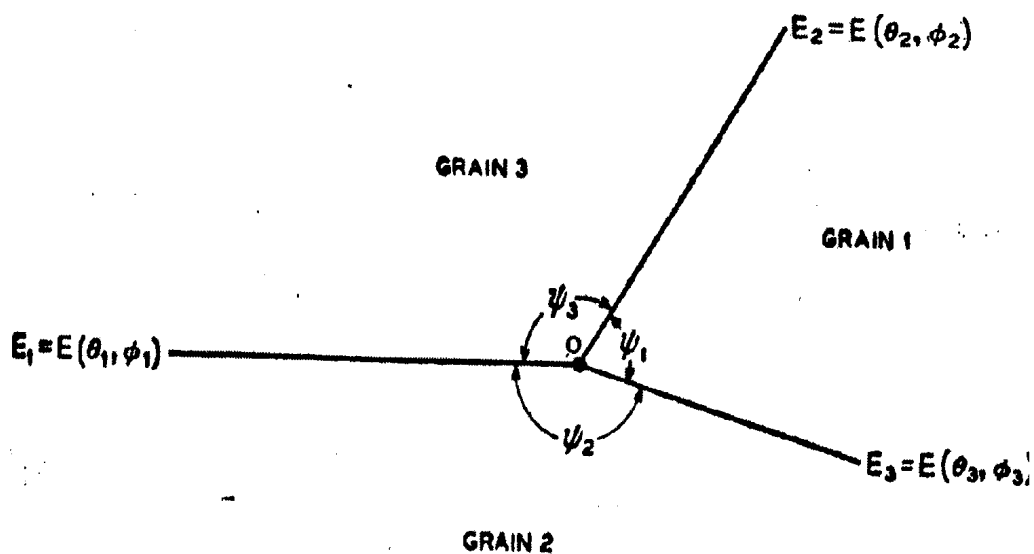
Figure 2.4: Three grain boundaries meeting along a line normal to the figure. Each boundary is defined in terms of a misorientation "tilt"angle θ and ""twist" angle Φ. The magnitudes of the angles Ψi indicate the relative energy of the grain boundaries according to equation 2.18 [19].

Figure 2.5 shows a plot of the relative grain boundary energy versus grain boundary misorientation measured from the tricrystals of iron, tin, and lead. The experimental data fall on the E vs θ trend predicted by Equation 2.17 for values of θ less than 30°. When the angular misorientation of the boundaries exceeds about 30°, Equation 2.17 does not predict well the measured relative energy. Although the data in Figure 2.5 where θ consisted of a simple rotation of the crystal about one axis, Read [19] has shown that Equation 2.17 holds for "general" grain boundaries where θ is the total angular rotation resulting from rotation about any axis.
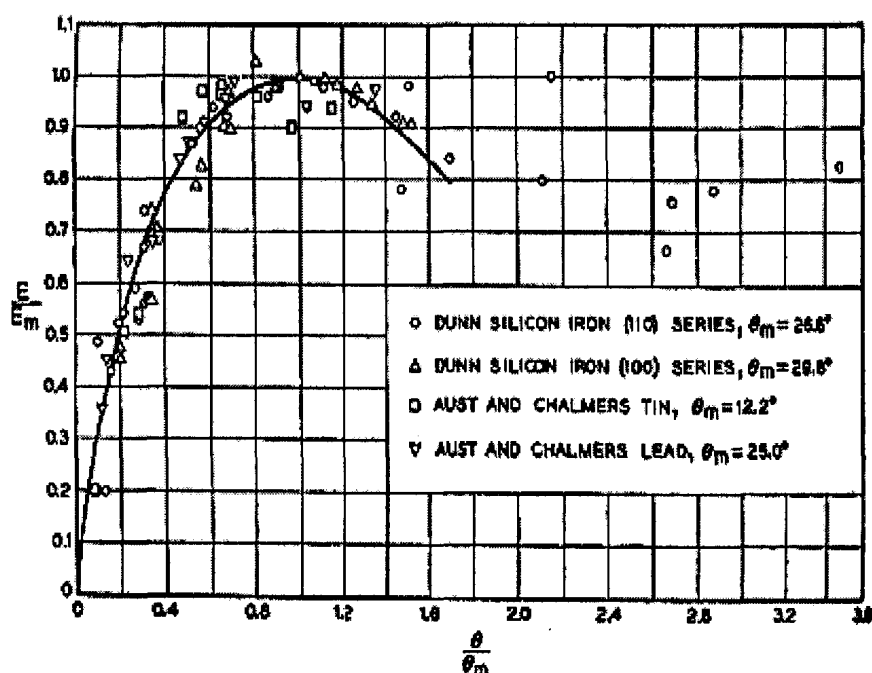
Figure 2.5: Relative grain boundary energy versus grain boundary misorientation measured from the tricrystals of iron, tin, and lead. When θ is small (less than 30°) the experimental data fall on the theoretical curve predicted by Equation 2.17 [19].

Since the rate of plastic deformation of most metals at room temperature is governed by the mechanism of obstacle-limited dislocation glide and is ultimately limited by the magnitude of the activation energy, ΔG_0, of the obstacles (Equation 2.5 and Table 2.1), it

seems reasonable that the energy of a grain boundary, as expressed by the Shockley-Read equation (Equation 2.17) will effect the local plastic strain rate in the vicinity of the grain boundary. In Chapter 5 data are presented from nanoindentation creep tests performed on, or very near to, grain boundaries of various levels of θ to study the influence of grain boundary misorientation on the deformation kinetics.

2.4 Electron Back Scattered Diffraction as a way to measure Crystallographic Orientation

Chapter 5 of this thesis describes an investigation of both grain orientation and grain boundary misorientaton on the rate of nanoindentation creep. This investigation necessitates a means for measuring local orientation of grains within the polycrystalline material being indented. Electron Back Scattered diffraction (EBSD) was used to accomplish this. This section deals with a review of published literature regarding the EBSD technique and the basis of using the data to determine crystallographic orientation.

2.4.1 EBSD - Basics
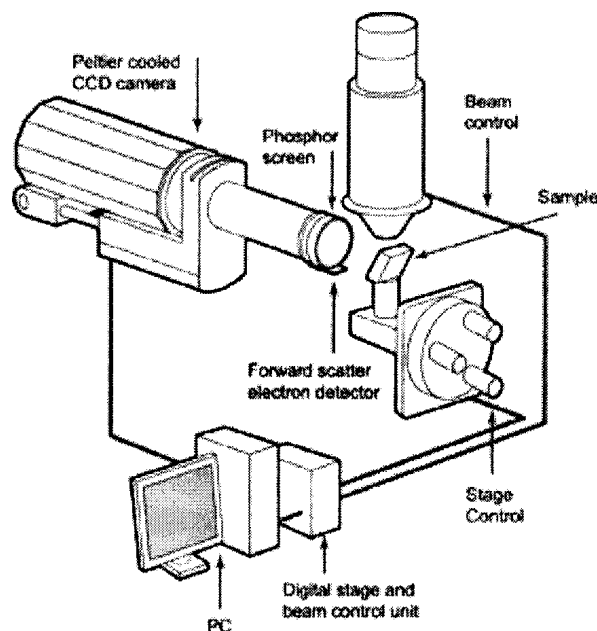
Figure 2.6: A schematic diagram of the basic component of an EBSD unit. [20]

Electron Backscatter Diffraction is a well-established technique by which crystallographic information can be obtained from samples in the scanning electron microscope (SEM). The basic components of an EBSD system are: a sample preferably tilted at about 70° from the horizontal, a phosphor screen that will be fluoresced by back scattered electrons eminating from the sample to form the diffraction pattern, a sensitive charge coupled device (CCD) video camera for viewing the diffraction pattern on the phosphor screen, a vacuum interface that allows for mounting of the phosphor screen and CCD camera in an SEM port, electronic hardware that controls the SEM, including the beam position, specimen stage movement, focus, and magnification (Figure 2.6) [20].

In the EBSD technique a stationary electron beam is directed upon a specific region of a tilted crystalline sample and undergoes elastic scattering from the surface atoms of the sample. The intensity of the back-scattered electrons depends upon their incident angle θ to the sample surface. At certain characteristic angles, θ_B, the back-scattered electron intensity reaches a maximum and this angle is related to the interplanar spacing, d, of a family of crystal planes in the sample by the famous Bragg's law:

$$n\lambda = 2dSin\theta_B \qquad (2.19)$$

where n is an integer, and λ is the wavelength of the incident electrons. During EBSD of a crystalline material the back-scattered electron intensity creates a series of parallel lines of high intensity on the phosphor screen (Figure 2.7). These bands are refered to a Kikuchi patterns. The width of the Kikuchi bands and their angular relationships to each other can be used to index the crystal orientation of the sample surface at the point where it is hit by the incident electron beam. The crystal orientation is typically indexed at each point by scanning the beam in a grid across a sample surface. The resulting map reveals the constituent grain morphology, orientations, and boundaries. In our investigation (Chapter 5) "EBSD automatic indexing software: HKL Systems" was used to process the Kikuchi pattern to result in the orientation solutions.
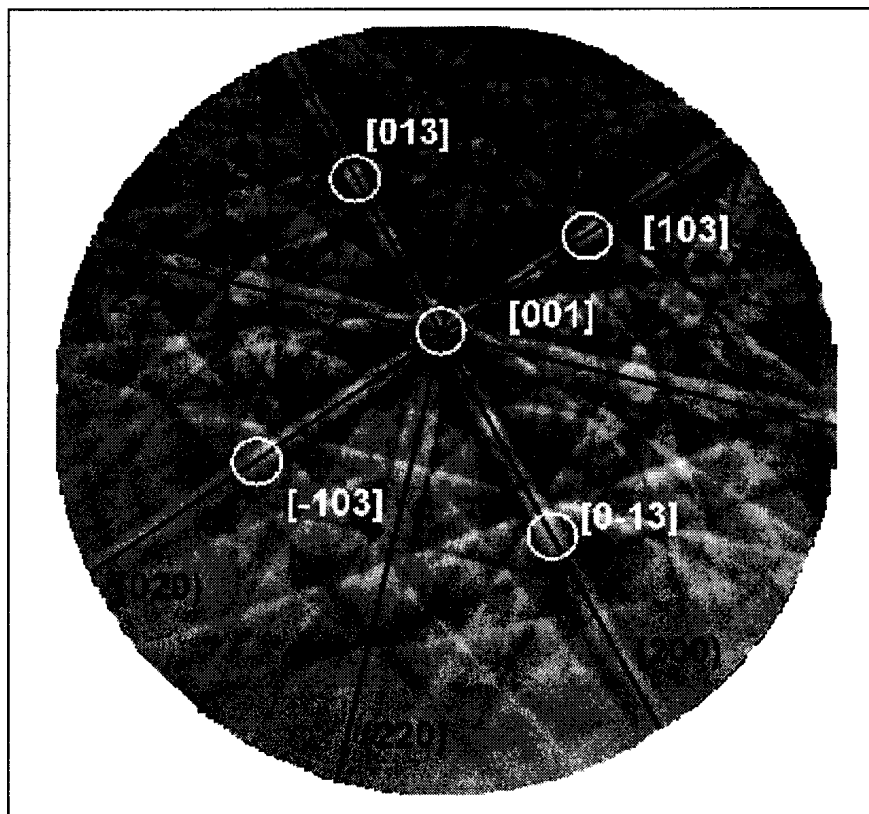
Figure 2.7: The indexing of the diffraction pattern of nickel is shown in this figure. Kikuchi bands are labeled with the Miller indices of the crystal planes that generated them (black). The planes project onto the screen at the center of the bands. Kikuchi band intersections are labeled with crystal direction that meets the screen at this point (white). This direction is the zone axis of the planes corresponding to the intersecting Kikuchi bands [20].

2.4.2 Description of a crystal orientation via Euler angles

This segment gives a brief description of the Euler angles used to represent crystallographic orientation. The Euler angles refer to sequential three-step rotations that transform the specimen coordinate system into the crystal coordinate system. According to Bunge's specification, the three rotations are:

1st a rotation of φ_1 about the crystal 001 (Z) axis

2nd a rotation of ϕ about the crystal 100 (X) axis

3rd a rotation of φ_2 about the crystal 001 (Z) axis [21]

Here, φ_1, ϕ, φ_2 are the Euler angles. The sequence of the three rotations is shown in Figure 2.8
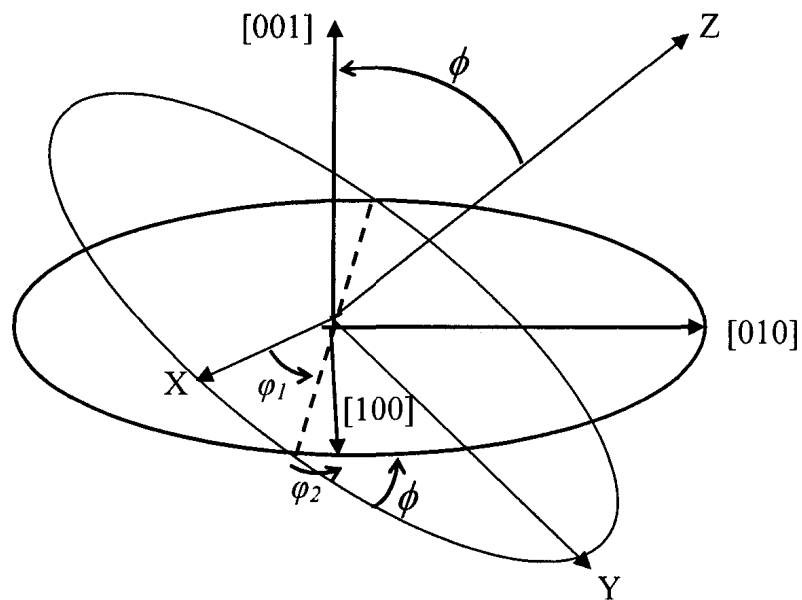
Figure 2.8: Schematic illustration of the three rotation between the specimen and crystal axes through φ_1, ϕ, φ_2 [22].

The three rotations can be expressed by three matrices as followed:

$$g_{\varphi_1} = \begin{pmatrix} \cos\varphi_1 & \sin\varphi_1 & 0 \\ -\sin\varphi_1 & \cos\varphi_1 & 0 \\ 0 & 0 & 1 \end{pmatrix}$$

$$g_\phi = \begin{pmatrix} 1 & 0 & 0 \\ 0 & \cos\phi & \sin\phi \\ 0 & -\sin\phi & \cos\phi \end{pmatrix} \tag{2.20}$$

$$g_{\varphi_2} = \begin{pmatrix} \cos\varphi_2 & \sin\varphi_2 & 0 \\ -\sin\varphi_2 & \cos\varphi_2 & 0 \\ 0 & 0 & 1 \end{pmatrix}$$

Multiplication of these three matrices in order gives the relationship between the orientation matrix and the Euler angles:

$$g = g_{\varphi_1} \cdot g_\phi \cdot g_{\varphi_2} \tag{2.21}$$

The elements of the matrix in terms of Euler angles can be expressed as:

$$g_{11} = \cos\varphi_1 \cos\varphi_2 - \sin\varphi_1 \sin\varphi_2 \cos\phi$$

$$g_{12} = \sin\varphi_1 \cos\varphi_2 + \cos\varphi_1 \sin\varphi_2 \cos\phi$$

$$g_{13} = \sin\varphi_2 \sin\phi$$

$$g_{21} = -\cos\varphi_1 \sin\varphi_2 - \sin\varphi_1 \cos\varphi_2 \cos\phi$$

$$g_{22} = -\sin\varphi_1 \sin\varphi_2 + \cos\varphi_1 \cos\varphi_2 \cos\phi \tag{2.22}$$

$$g_{23} = \cos\varphi_2 \sin\phi$$

$$g_{31} = \sin\varphi_1 \sin\phi$$

$$g_{32} = -\cos\varphi_1 \sin\phi$$

$$g_{33} = \cos\phi$$

All the Euler angles described above are according to Bunge's definition [23]. However there are some variations in the choice of Eulers angles. Roe [24] suggested the 2nd

rotation to be about the crystal Y-axis rather than the X-axis described by Bunge. The set of Euler angles Roe proposed were ψ, θ, ϕ and the equivalence of these angles with those of Bunge's are:

$$\varphi_1 = \psi + \frac{\pi}{2} \qquad \phi = \theta \qquad \varphi_2 = \phi - \frac{\pi}{2} \qquad (2.23)$$

Euler angles used in this thesis are based on Roe's specification. These angles were used to interpret crystallographic planes, which were in turn correlated with the deformation parameters. MATLAB codes based on Equations 2.22 can be used to convert the Euler angles into respective (h,k,l) planes. For cubic systems the angles between two planes, such as (h_1,k_1,l_1) and (h_2,k_2,l_2) can be calculated using the following equation:

$$\theta = Cos^{-1}\left[\frac{h_1 h_2 + k_1 k_1 + l_1 l_2}{\left(h_1^2 + k_1^2 + l_1^2\right)^{1/2}\left(h_2^2 + k_2^2 + l_2^2\right)^{1/2}}\right] \qquad (2.24)$$

This is how the crystallographic planes and angle between the planes were determined in the investigation described in Chapter 5.

2.5   Heat Treatment of Aluminum alloys

The material used for all the investigations in this thesis is the Aluminum 2024 alloy. This alloy contains about 4 wt% Cu, 1.5 wt% Mg and 0.5 wt% Mn. The 2024 alloy is widely used for aircraft structures, such as wings, because of its superior fatigue resistance and strength/weight ratio. This alloy requires solution heat-treatment to obtain optimum properties; in the heat-treated condition mechanical properties are similar to, and sometimes exceed, those of mild steel. In some instances, artificial aging is employed to further increase the mechanical properties. The reasons for choosing this alloy for this thesis investigation is that it's microstructure and mechanical properties can be varied by

relatively simple heat treatment and that, because of its relatively low T_{melt}, it undergoes significant creep deformation during indentation at room temperature.

One of the main objectives of this thesis is to study the effect of second phase particles on the nanoindentation creep. Precipitation heat treatment of the 2024 alloy produces dense and finely dispersed particles throughout the matrix. The amount and the size of the precipitates can be varied by selecting the appropriate heat treatment conditions. The precipitate particles act as obstacles to the dislocation motion and thus strengthen the heat-teated alloy. Figure 2.9 shows a typical heat treatment cycle for the 2024 aluminum alloy. The individual components of the heat treatment are discussed below.
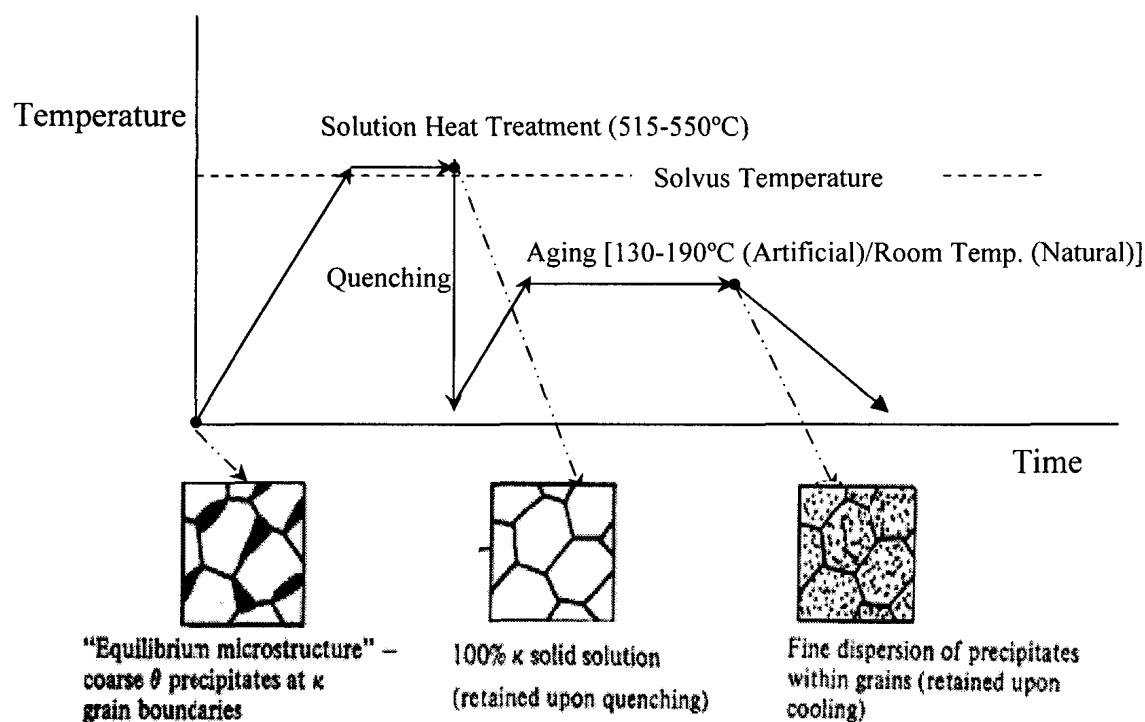
Figure 2.9: Typical Heat Treatment Cycle for 2024 aluminum alloys. A highly unstable supersaturated solid solution is produced by quenching the alloy from solutionizing temperature. Aging at low temperatures forms finely dispersed precipitates from the supersaturated quenched material. The size and amount of precipitates depends on the length of time of aging [26].

2.5.1 Solution Heat Treatment

This is the first step of the heat treatment process. In this step the aluminum alloy is heated to a temperature between the solvus and solidus temperatures and soaked at this temperature until a uniform solid solution structure is formed.

The solutionizing temperature of the 2024 alloy ranges from 515 to 550°C. The time required at the solution heat-treating temperature depends upon type and size of the sample. The soaking period will vary from 10 minutes for thin sheet to approximately 12 hours for the thicker materials, such as heavy forgings. A general guide to use is approximately 1-hour/inch of cross-sectional thickness.

2.5.2 Quenching

In this second step of the heat treatment process, the sample is rapidly cooled from the solution treatment temperature to room temperature. The cooling medium is usually water. The structure of the quenched alloy sample consists of a supersaturated solid solution.

2.5.3 Aging

Aging is the precipitation of solute atoms either at room temperature (natural aging) or at elevated temperature (artificial aging). The purpose of aging is to produce finely dispersed precipitates from the supersaturated quenched material. The fine precipitates act as obstacles to the dislocations during the deformation process. They force these dislocations to either pass through the precipitates or by pass around them. This causes the alloy to be strengthened.

2.6 Different Microstructures that can be formed by Aging of the 2024 Aluminum Alloy

Natural Aging

Natural aging is room temperature aging. In alloy 2024, most of the strengthening occurs within a day at room temperature; the mechanical properties are essentially stable after four days. No discernible microstructural changes accompany the room–temperature aging, since the hardening effects are attributable solely to the formation of zone structure within the solid solution. [25]

Artificial Aging

The 2024 alloy after solution heat treatment and quenching is artificially aged at 130-190°C [26]. The following five structures are usually formed sequentially during aging:

(1) Supersaturated solid-solution α

(2) GP1 zones

(3) GP2 zones (also called θ'' phase)

(4) θ' phase, and

(5) θ phase, $CuAl_2$.

Not all of these phases can be produced at all aging temperatures; GP1 and GP2 zones are produced at lower aging temperatures, whereas θ' and θ phases are produced at higher temperatures [25]. Figure 2.10 shows the Al-Cu binary phase diagram and the microstructures formed at different steps of the heat treatment process.
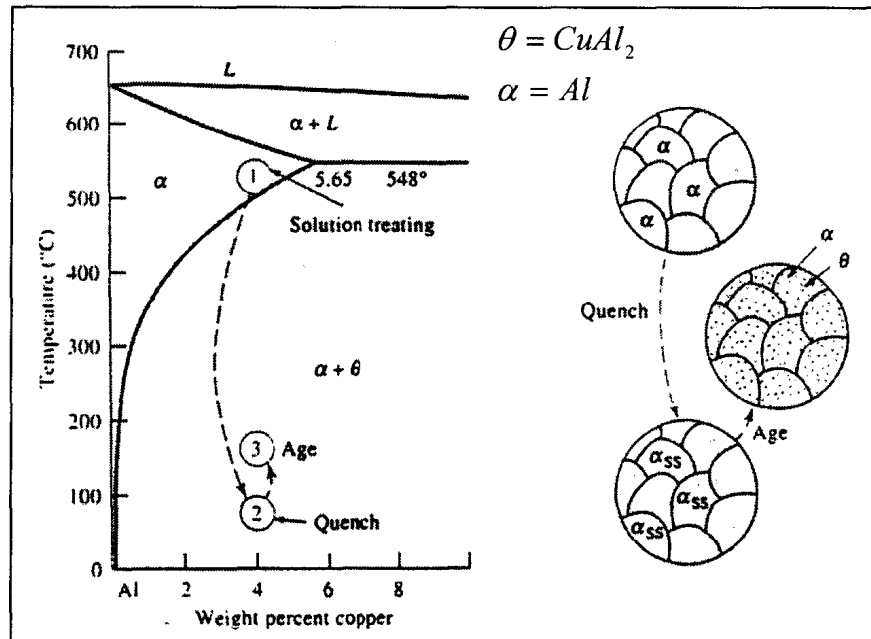
Figure 2.10: The Aluminum-Copper phase diagram showing the three steps in the heat-treatment process for a 2024 aluminum alloy and the microstructures that result. [26]

GP1 zones

At lower aging temperatures, copper atoms segregate in the supersaturated solid solution α and form GP1 zones. These zones consist of segregated regions having shape of disks that have thickness about 0.4-0.6nm and diameter about 8 to 10 nm. They are formed on the {100} cubic planes of the α matrix. Since the diameter of the copper atoms are about 11% less than the aluminum atoms, the matrix lattice around the zones is strained tetragonally. Since the copper atoms just replace aluminum atoms in the lattice, GP1 zones are essentially coherent (Fig. 2.11b). GP1 zones are detected with transmission electron microscopy by the elastic strain field contrast that they create (Figure 2.12a). [25]

GP2 zones (θ″ phase)

As aging proceeds the GP1 zones thicken into thin disks called GP2 zones. These zones also have a tetragonal structure which are coherent with the {100} of the matrix of the 2024 aluminum alloy. The size of these zones ranges from about 1-4nm thick to 10-100nm in diameter and increase with increasing aging time (Figure 2.12b) [26].

(a)   (b)
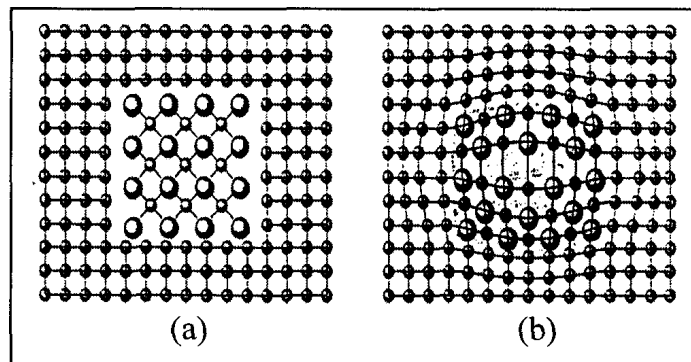
Figure 2.11: (a) An incoherent precipitate has no relationship with the crystal structure of the surrounding matrix. (b) A coherent precipitate has a definite relationship to the surrounding matrix crystal structure. [27]

θ′ phase

This phase nucleates heterogeneously at longer aging times. It is also incoherent (Fig.2.11a) with the matrix. θ′ phase has a tetragonal structure with a thickness ranging from 10nm to 150nm (Figure 2.12c) [26].

θ phase

After aging for a sufficiently longer period of time θ phase particles are formed. The θ phase is incoherent with the surrounding matrix. It has the composition $CuAl_2$. This phase has a Body Centered Tetragonal (BCT) unit cell with a=0.607nm and c=0.487nm.

(a) Heated to 540°C, water-quenched and aged 16h at 130°C. The GP zones formed as disks parallel to the {100} planes of the FCC matrix are now a few atoms thick and about 100Å in diameter.

(b) Solution treated at 540°C, water-quenched and aged 1day at 130°C. The thin-foil micrograph shows strain fields due to coherent GP2 zones. Elastic strain contrast causes the dark regions surrounding the zones.
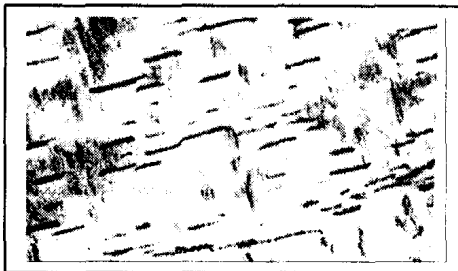
(c) Solution treated at 540°C, water-quenched and aged 3 days at 200°C. The micrograph shows incoherent and meta-stable phase θ' formed by heterogeneous nucleation and growth.

Figure 2.12: Changes in microstructure at different times and temperatures of Aging of a 2024 aluminum alloy [26].

In summary, during the aging treatment of the 2024 aluminum alloy the general sequence of precipitation that occurs is:

Supersaturated solid α solution $\rightarrow$ GP1 zones $\rightarrow$ GP2 zones (θ'' phase) $\rightarrow$ θ' $\rightarrow$ θ ($CuAl_2$) [26]

2.7 Structure-Hardness Correlations in a Heat-Treated 2024 Aluminum Alloy

Fig. 2.13 shows how the hardness changes with aging time for a 2024 aluminum alloy aged at 130 and 190°C. At 130°C, GP1 zones are formed. The hardness of the alloy increases as the dislocation movement is impeded by these zones. Further aging at 130°C produces GP2 zones that make the dislocation movement more difficult and result in a further increase in hardness. With further increasing aging time at 130^0C, a maximum hardness is reached as θ' forms. Aging beyond the highest hardness coarsens the θ' phase and dissolves the GP2 zones. This causes a decrease in the hardness. During aging at 190°C, GP1 zones do not form since this temperature is above the GP1 solvus. With long aging times at 190°C the equilibrium θ phase forms and the hardness is decreased. [26] Figure 2.13 therefore illustrates how lower aging temperatures can promote the precipitation of the θ' phase which results in far superior hardness than the GP1 phase. One drawback to using lower aging temperatures is that the precipitation kinetics are slowed resulting in peak hardness after nearly 100 days at 130°C compared to about 1 day at 190°C. For this reason, Chapter 4 presents data on the effects of precipitates on the indentation creep rates of the 2024 aluminum alloy heat-treated for different length of time at 190°C (470K) rather than 130°C.
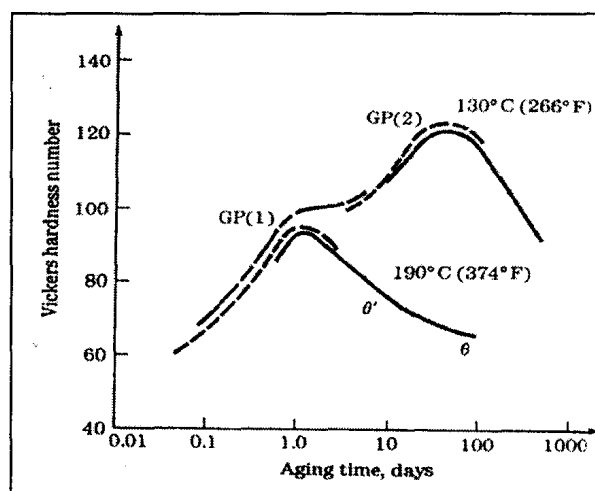
Figure 2.13: Correlation of microstructure and hardness of the 2024 aluminum alloy aged at 130°C and 190°C [26]

References

1. Argon A.S., *Scripta Met.*, v.4 (1970), p.1001

2. Hull D., Bacon D.J., *"Introduction to dislocations"*, Fourth edition (2005), Elsevier Butterworth-Heinemann, Oxford (England)

3. Kocks U.F., Argon A.S., Ashby M.F., *Prog. Mat. Sci.*, v.19 (1975)

4. Frost H.J., Ashby M.F., *"Deformation Mechanism Maps"*, Pergamon Press (1982), Oxford (England)

5. Guyot P., Dorn J.E., *Can. J. Phys.*, v. 45 (1967), p. 983

6. Hirth J.P., Lothe J., *"Theory of Dislocations"*, McGraw Hill (1968), New York

7. Kurzydlowski K.J., Ralph. B., Bucki J.J., Garbacz A., *Materials Science and Engineering*, v. 205 (1996), p. 127

8. Lasalmonie A., Strudel J, *J. Mater.Sci.*, v. 21 (1986), p. 1817

9. Petch N.J., *J. Iron Steel Inst.*, v. 174 (1953), p. 25

10. Hall, E.O., *Proc. Phys. Soc.* B, v. 64 (1951), p. 747

11. Lim Y.Y. and Chaudhri M. M., *Philosophical Magazine A*, v. 82 (2002), p. 2071

12. Armstrong R., Codd I., Douthwaite R.M., Petch N.J., *Philosophical Magazine*, v. 11 (1962), p. 45.

13. Hansen N., Ralph B., *Acta Metall.*, v30 (1982), p. 411

14. E. Schweitzer, K. Durst, D. Amberger, M. Göken, *Mat. Res. Soc. Symp. Proc.* v. 821 (2004), p. 163

15. Chang S.Y., Chang T.K., *Journal of Applied Physics*, v. 101 (2007)

16. Kumar K.S., Swygenhoven H. V., Suresh S., *Acta Mater.*, v.51(2003), p. 5743

17. Read W.T. and Shockley W., *Phys. Rev.*, v. 78 (1950), p. 275

18. Read W.T. and Shockley W., *"Imperfections in Nearly Perfect Crystals"*, (W. Shockley edition), Ch. 13, Wiley (1952), New York

19. Read, W.T., *"Dislocations in Crystals"*, McGraw Hill (1953), New York

20. http://www.ebsd.com/ebsdexplained.htm as of 10 pm, July 17, 2007.

21. Randle V., Englar O.," *Introduction to Texture Analysis: Macrotexture, Microtexture and Orientation Mapping"*, Gordon and Breach (2000), Amsterdam

22. Randle V., *"Microstructure Determination and its Application"*, The institute of Materials (1992), London

23. Bunge H. J.; translated by Morris Peter R. *"Texture analysis in materials science: mathematical methods"*, Butterworths (1982) London

24. Roe R.J., *Journal of Applied Physics,* v. 36 (1965), p. 2024

25. Silcock J.M., Heal T.J., Hardy H.K., *"Aluminum"* (edited by Van Horn K.R.), v.1 (1967), American Society for Metals

26. Smith W. F., *"Foundation of Materials Science and Engineering"*, McGraw Hill (2004), New York

27. Askeland D.R., *"The science and engineering of materials"*, (3rd S.I. edition), Stanley Thornes (1998), Cheltenham

Chapter 3

Nanoindentation Testing

Since the objective of this thesis is to use the nanoindentation creep test to study the effect of microstructural features on the mechanisms of local plastic deformation within a heat treated aluminum alloy, it is important to review the underlying theory of the indentation testing technique.

Nanoindentation testing involves pressing a small, rigid, indenter against a flat surface of the test material. If the shape of the indenter is known, the projected area of the indentation on the sample surface can be calculated from the indentation depth. The applied indentation force divided by this projected area is the average indentation stress which is related to the flow stress of the test material. Since a nanoindentation only penetrates into the test material to the depths typically less than1 μm, the average indentation stress reflects the local flow properties of a very small volume of the test material, near the free surface. These local flow properties can be considerably different than the flow properties of the bulk material.

If a constant force indentation test is performed for an extended period of time the indentation depth will increase with time as the indenter sinks into the test material through a process of time-dependent "creep" deformation. By monitoring the rate at which the indentation depth increases the local time-dependent flow properties of small volumes of the test material can be studied. This is the objective of the studies presented in this thesis.

What follows is a description of the various components of the Micro-Materials Nano-test platform used to perform the indentation creep tests described in Chapters 4 and 5. Section 3.1 describes the geometry of the Berkovich indenter that was used in the investigations along with the resulting equations describing contact area and the average

indentation stress. A description of the overall indentation tester follows in Section 3.2. Finally, a description is given in Section 3.3 of the methods used to analyze the indentation force and depth data resulting from constant load nanoindentation creep tests.

3.1 The Berkovich Indenter

The main requirements for a suitable indenter for a nanoindentation test are low friction with the indented material, no plastic deformation, smooth surface and high elastic modulus. Choosing diamond for the indenter tip satisfies these requirements. Another main requirement is a very precise indenter point with a radius in the order of 100nm. This requirement is satisfied by using Berkovich indenter geometry. A Berkovich indenter is a three-sided pyramid usually constructed from a diamond crystal by a grinding operation. The three-sided geometry ensures that a sharp pointed tip can be made. The Berkovich indenter has a much sharper tip than the four-sided Vickers indenters that are commonly used for micro-indentation testing [2].

The Berkovich indenter geometry is shown in Figure 3.1. It has a triangular base with three triangular faces inclined at an angle of 65.3° with respect to the vertical axis (Figure 3.1 a). The radius of the tip of the pyramid is typically less than 100nm. The impression made by a Berkovich indenter appears as an equilateral triangle (Fig. 3.1b). The projected area, A, of the triangle is related to the indentation depth h, and the face angle θ by the following equation:

$$A = 3 \sqrt{3}\ h^2 \tan^2 \theta \qquad (3.1)$$

Since $\theta = 65.3°$, A is expressed in terms of h as

$$A = 24.5\ h^2 \qquad (3.2)$$

The mean indentation contact pressure or stress is expressed as:

$$\sigma_{ind} = \frac{Indentation\ Force}{24.5h^2}$$

(3.3)
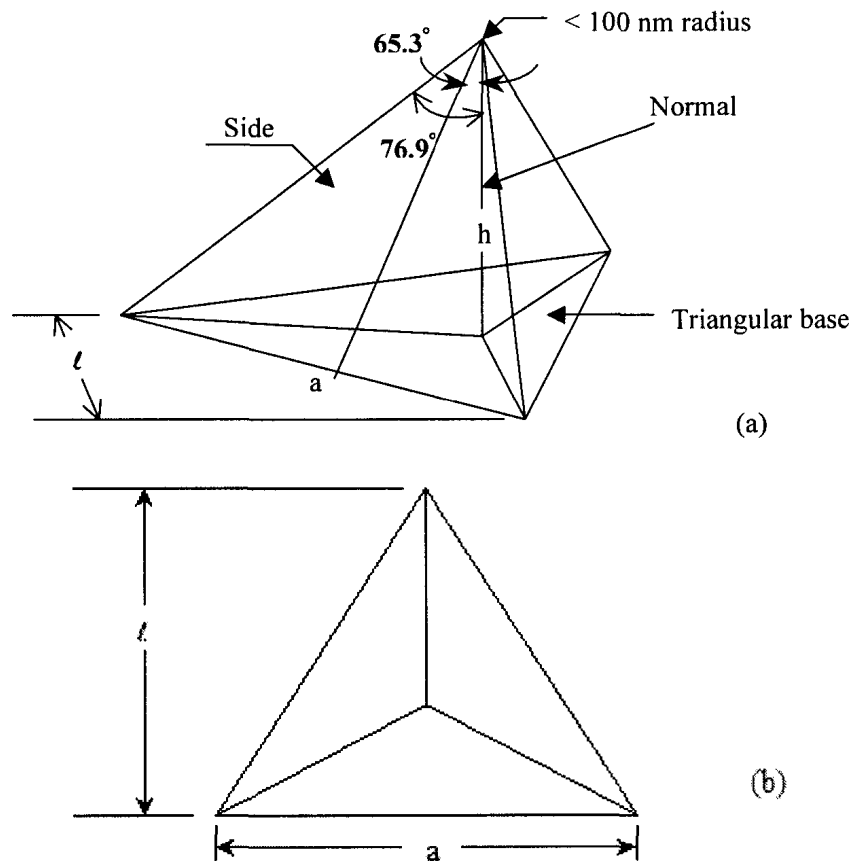
Figure 3.1: Schematic diagram of (a) a Berkovich indenter and (b) an impression an indentation made by a Berkovich tip indented on a flat surface [1].

3.2 The Nano Test Platform

All the nano-indentation tests in this study were performed using a computer controlled Micro Materials NanoTest indentation-testing platform made by Micro Materials Ltd., Wrexham, UK. Figure 3.2 shows a schematic diagram of this instrument [Original design - University of Lancaster, UK, Newey, Wilkins and Pollock, J Phys E, 1982, pp119-122.

Micro Materials formed 1988 by Dr Jim Smith, first instruments sold 1992]. The heart of the instrument is a ceramic pendulum that is mounted vertically. An electromagnetic coil wrapped around an aluminum core is attached to the upper end of the pendulum. The pendulum rotates about a pivot located at its mid-height. The bottom end of the pendulum contains the holder upon which the diamond Berkovich indenter is attached. When electric current is supplied to the coil, the core is magnetized and is attracted to the nearby permanent magnet. This causes the pendulum to rotate and the indenter to move toward the sample. A parallel capacitor plate located behind the indenter measures the movement of the indenter. A computer system is interfaced with this nanoindenter and controls the indentation process by controlling the electrical current fed to the coil. The indentation force is a function of the magnitude of this current. The indentation depth is related to the capacitance measured across the parallel capacitor plates. Both the relationships between indentation force and coil current and indenter displacement and capacitance are determined by calibration tests performed frequently during the course of indentation testing.
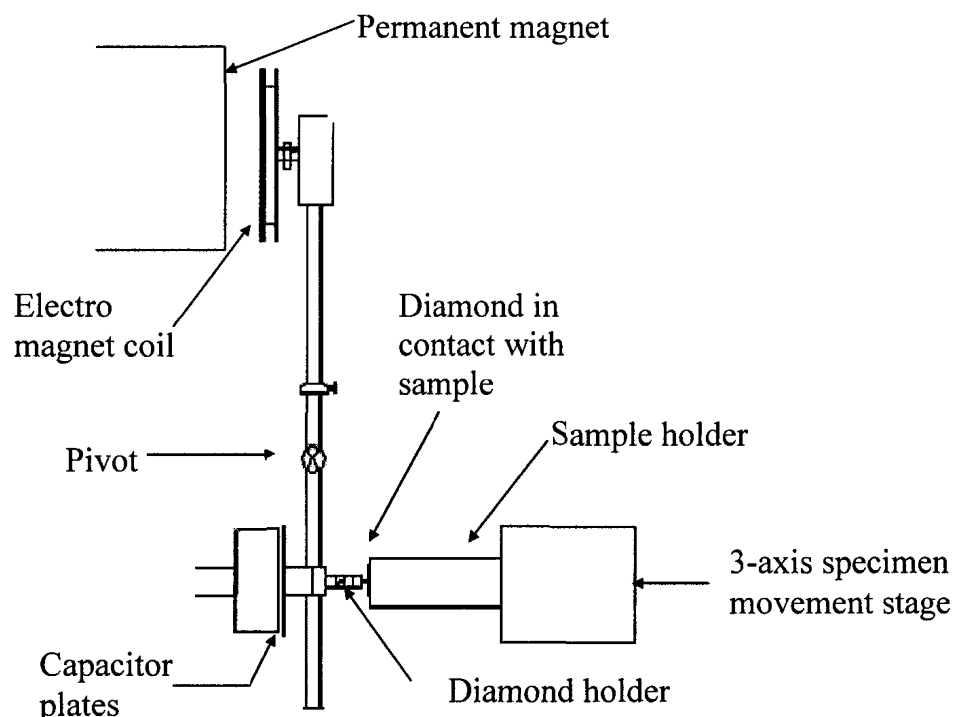
Figure 3.2: Schematic diagram of a NanoTest Platform assembly.

An indentation load up to 500mN can be applied with this nano test instrument and the force resolution is better than ±100nN. Maximum Depth of 100 μm can be achieved with a depth resolution less than ±0.1 nm. The XYZ mechanical translation stage containing the sample stage can be moved up to 200mm in X and Y direction and 20 mm in the Z direction. The positional resolution of each of the stage axes is ±1μm.

Software is used to control all indentation tests. It allows positioning the sample stage, finding the sample surface, specifying different parameters such as loading and unloading rates, indentation depth, and length of time etc.

For this particular thesis the nano test instrument was used primarily for constant load indentation creep test, where the maximum load to reach a required initial indentation depth was kept constant for one hour, the software measures the indentation depths at 18 seconds intervals. The results were corrected, using the NanoTest software, for both thermal drift and elastic compliance of the indentation tester.

3.3 Indentation Data Analysis

Force, displacement and time are measured continuously throughout a test performed with the Nano-test instrument. An indentation creep test gives a curve that shows the relationship between Force, F and indentation depth, h. The measured h includes contributions from both the elastic and plastic deformation of the indented material. On unloading, a sloped rather than a vertical unloading curve is produced as the elastic component of the displacement recovers. A typical indentation force versus depth curve for a constant load pyramidal indentation test is shown in Figure 3.3. The elastic modulus of the specimen is measured by fitting a straight line that is tangent to the unloading curve at the maximum load and then measuring the slope of the fitted straight line as shown in the figure.
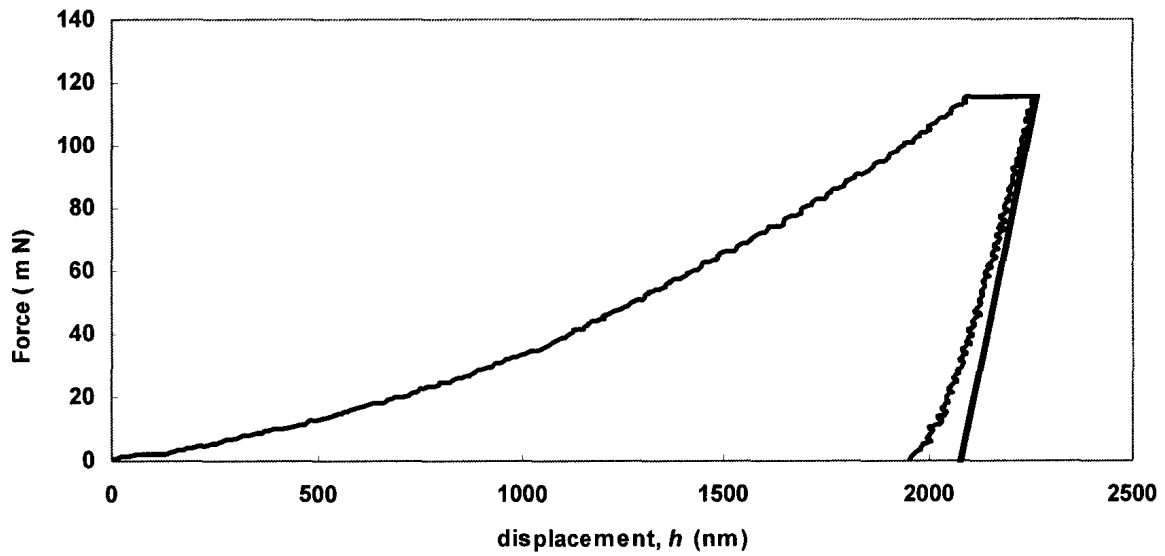
Figure 3.3: Typical load-displacement curve. During the tests, the indentation load is increased to reach the desired h_0. The indentation load is then held constant for one hour. The horizontal part of the curve shows the amount of creep that occurs during the one-hour test period. The elastic modulus of the specimen can be measured by fitting a straight-line tangent to the unloading curve at the maximum load [2].
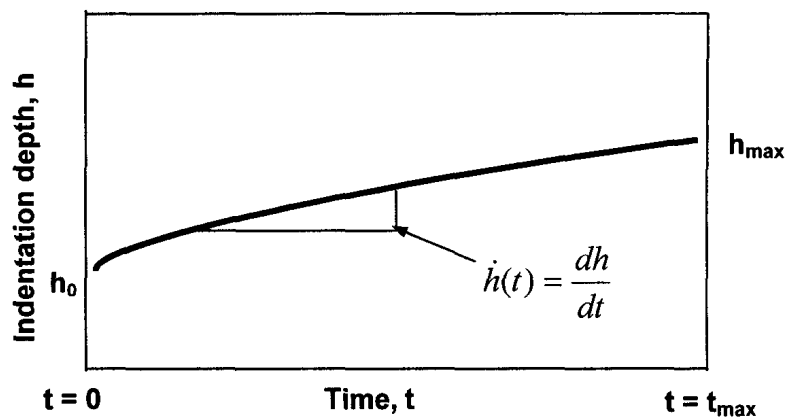
Figure 3.4: Diagram of a typical indentation depth versus time plot obtained from a constant load indentation test.

One-hour, constant-load indentation tests are performed by loading a specimen to a predetermined load to reach the required indentation depth and then keeping the load constant for one hour. During the constant-load time period, the indentation depth is recorded every 18 seconds. Figure 3.4 shows a plot of a typical indentation depth versus time curve.
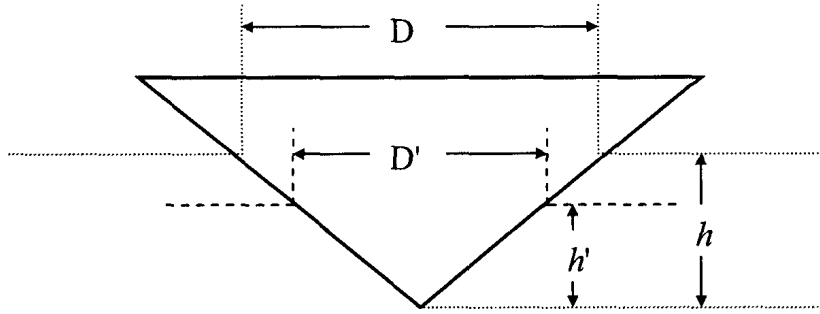
Figure 3.5: Schematic diagram of geometrically self-similarity of a pyramid indenter.

For a self-similar indent the ratio D/h (Figure 3.5) is always constant regardless of the magnitude of h. As the average indentation strain is a function of D/h, it remains constant, regardless of indentation depth, due to the self-similar geometry of the Berkovich indenter. However, the average indentation strain rate changes with time. Indentation strain rate is a ratio of the indentation velocity, $\dot{h}(t)$, to the instantaneous indentation depth, $h(t)$ and can be expressed as

$$\dot{\varepsilon}_{ind} = K \frac{\dot{h}(t)}{h(t)} \tag{3.6}$$

where the constant K is related to both of the geometry of the indenter and the work hardening property of the indented material [3]. In most cases, researchers use K=1 and refer to $\dot{\varepsilon}_{ind}$ as the nominal indentation strain rate.

When the indentation depth, h, is large (greater than several micrometers), the σ_{ind} measured by geometrically self-similar Berkovich indentation is essentially independent of h. This is not the case for nanoindentation where h is less than $1\,\mu m$. The σ_{ind} values measured by nanoindentation test increase with decreasing h. This is known as the indentation size effect [4] and has been studied extensively [4-10] with various mechanisms being proposed to explain the phenomenon. The most accepted mechanism applies the strain gradient plasticity theory [4-6] to suggest that large numbers of geometrically necessary dislocations resulting from the presence of a substantial strain gradient around nanometer depth indentations causes enhanced hardening which causes the observed increase in σ_{ind} [11].

References

1. Bhushan, B.; Gupta, B.K., *"Handbbok of Hard Coatings - Deposition Technologies, Properties and Applications"*, (Bunshah R.F. Ed), Noyes Publications (2001), New Jersey, USA, p. 550.

2. AC Fischer-Cripps, *"Nanoindentation"* (2nd edition), Springer (2004), New York, p. 27

3. Johnson KL, *J. Mech. Phys. Solids,* v. 18 (1970), p. 115

4. Fleck N.A., Mullar G.M., Ashby M.F., Hutchinson J.W., *Acta Metall. Mater.,* v.42 (1994), p. 475

5. Poole W.J., Ashby M.F., Fleck N.A., *Scripta Metall. Mater.* v.34 (1996), p. 559

6. Nix W. D., Gao H., *J. Mech. Phys. Solids,* v. 46 (1998), p. 411

7. Bhakhri V., Klassen R. J., *Scripta Mater.,* v. 55 (2006), p. 395

8. Elmustafa A. A., Stone D.S., *Materials Letters,* v. 57 (2003), p. 1072

9. Elmustafa A. A., Stone D.S., *Mater. Sci. Eng,* A, v. 358 (2003), p. 1

10. Elmustafa A. A., Stone D.S., *J. Mech. Phys. Solids,* v. 51 (2003), p.357

11. Ashby MF, *Phil. Mag.,* v. 21 (1970), p. 399

Chapter 4[*]

Dependence of the nanoindentation creep rate of heat-treated 2024 aluminum at 300K upon indentation depth

4.1   Introduction

Creep deformation during constant-load pyramidal microindentation has been investigated in a variety of metals [1-4]. The average indentation stress, σ_{ind}, during such tests decreases with time as the indentation depth increases due to creep deformation. σ_{ind} is proportional to the flow stress of the material; therefore, the decreasing σ_{ind} indicates that the creep deformation results in a changing dislocation structure within the indentation plastic zone. If one considers the flow stress to be inversely proportional to the spacing of the obstacles to dislocation glide, the observed decrease in σ_{ind} suggests that the inter-obstacle spacing in the indentation plastic zone increases as a result of constant-load indentation creep.

During constant-load pyramidal indentation creep tests, a threshold indentation stress, σ_{th}, is inevitably reached below which negligible indentation creep occurs. The magnitude of σ_{th} has been shown to be a function of the microstructure in high-temperature microindentation creep tests performed on aluminum alloys and aluminum-based composites [5-6].

The local stress ahead of a pyramidal indentation is very high and, as a result, indentation creep occurs by a deformation mechanism involving obstacle-limited dislocation glide [5-10]. Under these conditions the equivalent average indentation shear strain rate $\dot{\gamma}_{ind}$ can

be expressed in terms of the equivalent average effective indentation shear stress τ_{eff} and the temperature T as

$$\dot{\gamma}_{ind} = \dot{\gamma}_0 e^{-\Delta G(\tau_{eff})/kT} \tag{4.1}$$

where $\dot{\gamma}_0$ is a material constant, k is the Boltzmann's constant, and $\Delta G(\tau_{eff})$ is the thermal energy required for a dislocation, subjected to τ_{eff}, to overcome and glide past the deformation rate limiting obstacle. Constant-load indentation creep tests performed on gold, aluminum alloys, and aluminum-based composites have indicated that the total thermal activation energy, ΔG_0, of the deformation rate limiting obstacles is within the range expected for "weak" obstacle such as dislocation/dislocation interactions [5-7].

Recent investigation of the dependence of $\Delta G(\tau_{eff})$ on indentation depth h in polycrystalline gold at 300K has shown that, although the dislocation density in the indentation zone is a function of indentation depth, ΔG_0 and σ_{th} are essentially independent of indentation depth [7]. This finding may not be surprising when one considers the indentation creep of a pure metal, such as gold, where a deformation mechanism involving simple dislocation/dislocation interactions is expected to control the creep rate. However it raises the question of whether the presence of alloying elements results in a different value of ΔG_0 that might be dependent upon indentation depth. This question addresses the nature of the interactions between geometrically necessary dislocations and obstacles, such as second phase precipitates, in the indentation depth range were the hardness of the material is known to be depth dependent.

We present here the results of a study on the effect of heat treatment on the indentation depth dependence of σ_{th} and ΔG_0 of a 2024 aluminum alloy in the as-quenched, peak-aged, and over-aged conditions at 300K. This alloy was chosen for this investigation because it can be hardened very effectively by simple heat treatments and because it undergoes significant indentation creep at 300 K.

4.2 Procedure

Samples of commercial purity 2024 aluminum, 25.4 mm in diameter and 12 mm thickness, were solution treated at 810 K for 24 hours and then water quenched. Individual as-quenched samples were then aged at 460 K for 1, 2, 5, 10, 15, 24, 28, 48, 240, 288 and 360 hours. The Vickers microhardness of the samples was then measured (Fig. 4.1). The material displays a peak hardness of 150 VHN after 15 hours at 460 K.

Samples from the as-quenched, peak-aged, and over-aged (360 hours) conditions were mechanically polished to a 0.05 μm surface finish and then electropolished in a solution of 74 vol% orthophosphoric acid, 12 vol% sulphuric acid, 9 vol% distilled water and 5 vol% chromium trioxide. The average roughness of the electropolished surface was measured with an atomic force microscope and was about ± 10 nm in the regions where the indentation tests were performed (Fig. 4.2).
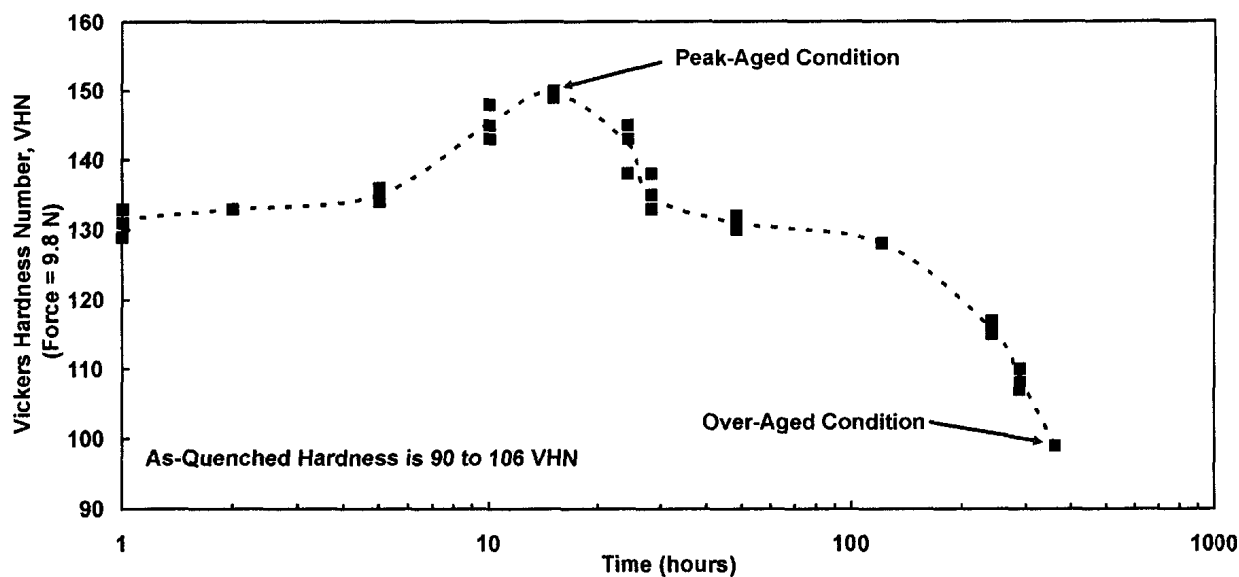
Figure 4.1: Vickers microhardness of the 2024 aluminum alloy versus aging time at 460K. The as-quenched, peak-aged, and over-aged conditions labelled on this figure indicated the thermal conditions tested in this investigation.

Between seven and twenty constant-load indentation creep tests were carried out at each of the following initial depths h_0 =: 100, 200, 300, 400, 500, 1000, 2000 nm on the as-quenched, peak-aged, and over-aged samples (Table 4.1). The as-quenched samples were prepared and tested immediately after quenching to minimize the amount of second phase precipitation occurring at room temperature prior to the creep tests.
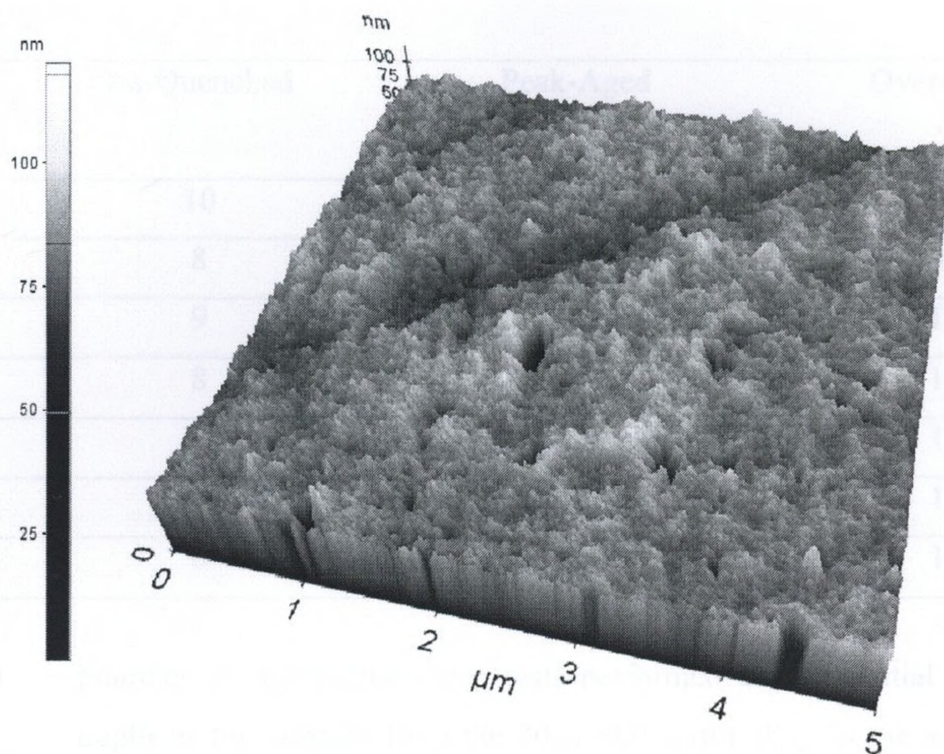
Figure 4.2 Atomic force microscopy image of the surface of a typical region of the electropolished 2024 aluminum alloy. The average surface roughness in the area where the nanoindentation creep tests were performed is about ± 10 nm.

Constant-load indentation creep tests were performed with a Micro Materials NanoTest indentation testing platform (Micro Materials Ltd., Wrexham, UK). A diamond Berkovich indenter was used for the tests. Each creep test began by first establishing the location of the specimen surface by indenting the sample with a small force of 0.1 mN. The indentation depth corresponding to this force was taken as the position of the sample surface. The indenter was then retracted and moved several micrometers from the point where the surface was detected. The indentation creep test was then performed by

increasing the indentation force until the h_0 at which the indentation creep test was to be performed was reached. The loading rate during the indentation was rapid and h_0 was reached in about 15 seconds. The indentation load was then held constant for one hour while h was recorded at 18 second intervals. The indentation depth was corrected for both thermal drift and compliance of the indentation tester. The thermal drift rate for all tests was less than 0.05 nm/s.

h_0 (nm)	As-Quenched	Peak-Aged	Over-Aged
100	10	12	10
200	8	10	8
300	9	20	10
400	8	7	14
500	7	13	12
1000	10	7	11
2000	6	9	13

Table 4.1   Number of indentation creep tests performed at each initial indentation depth h_0 for samples from the 2024 aluminum alloy in the as-quenched, peak-aged and over-aged conditions.

The average indentation stress, σ_{ind}, the average indentation strain rate $\dot{\varepsilon}_{ind}$, and the average effective indentation shear strain rate $\dot{\gamma}_{ind}$ were calculated from the h versus time data as:

$$\sigma_{ind} = \frac{F}{24.5\alpha h^2}, \quad \dot{\varepsilon}_{ind} = \frac{1}{h}\frac{dh}{dt}, \quad \dot{\gamma}_{ind} = \sqrt{3}\,\dot{\varepsilon}_{ind} \tag{4.2}$$

where F is the indentation force and α is a geometrical constant that accounts for the increase in the projected indentation area due to pile up. α was determined by measuring the projected indentation area from SEM micrographs of indentations made to various depths between 100 and 2000 nm and comparing this area to that of an ideally sharp

Berkovich indentation of the same depth. Figure 4.3 shows that the values of α at various indentation depths are independent of indentation depth.
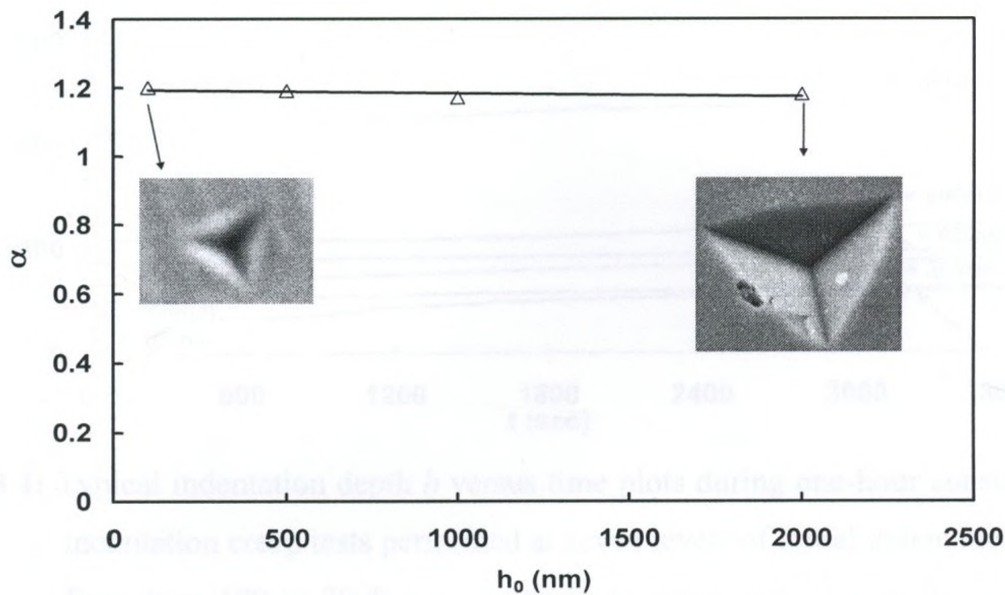
Figure 4.3: Typical α versus h_0 plot showing that α is not dependent upon h_0. The plot also consists of two SEM images of the indentations made at $h_0 = 100$nm and $h_0 = 2000$nm.

4.3 Results

Figure 4.4 shows h plotted versus time for several constant-load indentation creep tests performed on the peak-aged 2024 alloy. The as-quenched and the over-aged material showed similar trends of increasing h with time; however the magnitude of h was different for each heat treatment condition. For a given h_0 and time, the indentation creep rate (Eq. 4.2) is highest for the over-aged samples followed by the as-quenched and then the peak aged samples.
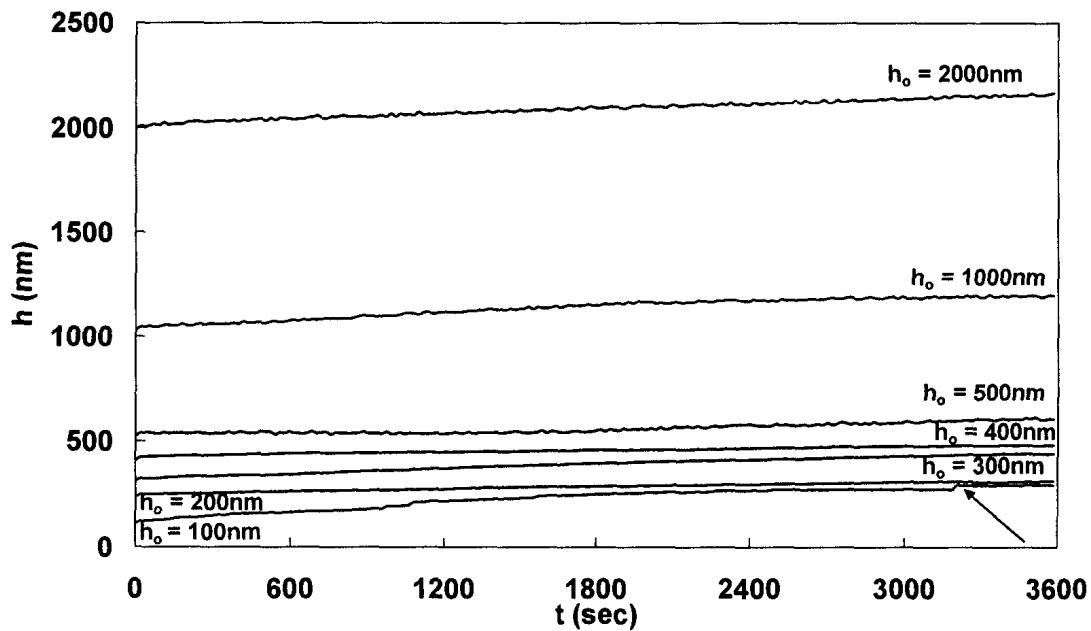
Figure 4.4: Typical indentation depth h versus time plots during one-hour constant-load indentation creep tests performed at seven levels of initial indentation depth, from h_0 = 100 to 2000 nm, on the 2024 aluminum alloy in the peak-aged condition. Considerable indentation creep takes place during the course of the tests. When h_0 is small (100 or 200 nm) the h versus time trend displays discontinuities (one of which is indicated by the arrow). The data from tests performed on the as-quenched and over-aged material show similar trends of increasing h with time however the magnitude of h was different.

The decrease in σ_{ind} (Eq. 4.2) with time during constant indentation load creep tests of the peak-aged material is shown in Fig. 4.5. The rate of stress relaxation is very high in the early stages of the tests, and the shallow indentations display higher relaxation rates than the deeper indentations. After one hour under constant indentation load the stress relaxation rate has decreased by more than two orders of magnitude to within the range of -0.38 to -0.05 MPa/s. We therefore take the average indentation stress after one hour under constant indentation load to be the apparent threshold indentation stress, σ_{th}, below which negligible further indentation creep occurs. The average initial indentation stress at the start of the constant load period, $\sigma_{ind(t=0)}$, and σ_{th} are labeled in Fig. 4.5 and were recorded for each indentation creep test to assess the dependence of the initial- and the crept- microstructures upon the indentation depth.
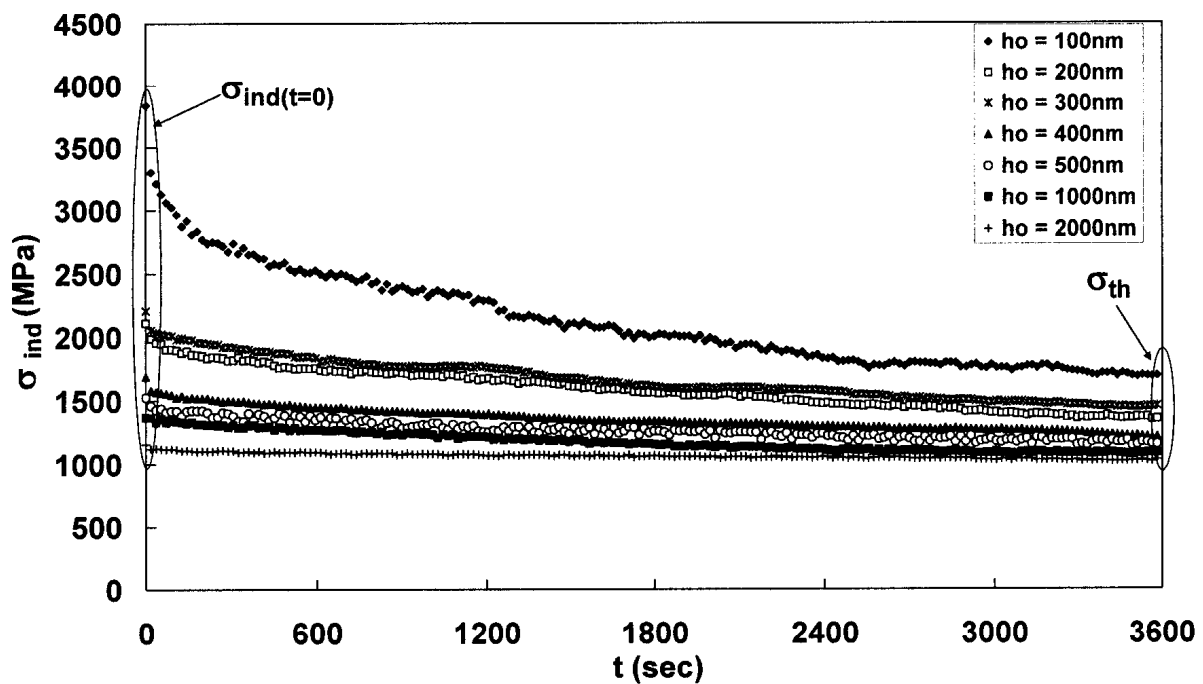
Figure 4.5: Average indentation stress σ_{ind} versus time for the same indentation creep tests shown in Fig. 4.4. σ_{ind} decreases at a high rate at the beginning of the test but, at the end of the creep test, approaches a value, σ_{th}, that is essentially constant with respect to time. The initial average indentation stress $\sigma_{ind(t=0)}$ and σ_{th}, labeled on the plot are proportional to the flow stress of the test material at the beginning and at the end of the creep tests respectively. They are therefore analyzed for their dependence upon indentation depth in Fig. 4.6.

Figure 4.6 shows $\sigma_{ind(t=0)}$ versus h_0 and σ_{th} versus the final indentation depth h_f. The scatter in the $\sigma_{ind(t=0)}$ and σ_{th} data increases considerably when the indentation depth decreases below 500 nm (Fig. 4.6). This is partly due to the effects of surface roughness, finite indentation tip radius, and the finite indentation depth resolution on the ability to accurately determine σ_{ind} when h is less than 500 nm. Post-test examination of the small indentations indicates that there also is also grain-to-grain variability in the indentation size. This suggests that when the indentation depth is small, and the deformation process occurs by the movement of a relatively small number of dislocations and the driving

stress required for indentation creep in this 2024 aluminum alloy is dependent upon the crystallographic direction of indentation. In addition to this, we observe that when h_0 is small, on the order of 100 or 200 nm, discontinuities are often seen in the h versus time plots. An example of one such "jump" in the h versus time is labeled in Fig. 4.5. The occurrence of such deformation discontinuities during conventional nanoindentation hardness testing has been reported previously [11]. We are presently studying the apparent crystallographic dependence of the nanoindentation stress and the effect of nonuniform dislocation motion during nanoindentation creep of a variety of metals. Despite these observations, all the constant load indentation creep tests that were performed in this study at depths below 500 nm show increasing h with time which, when analyzed, yield data suggesting that the creep process is occurring by an obstacle-limited dislocation glide mechanism (Section 4.4).

The data shown in Fig. 4.6(a) indicate that, despite the scatter described above, $\sigma_{ind(t=0)}$ clearly decreases from about 4000 to 1200 MPa as h_0 increases from 100 to 2000 nm. These findings are similar to previously reported data on the depth dependence of the indentation hardness of a naturally aged 2024 aluminum alloy [12]. The difference in the indentation depth dependence of $\sigma_{ind(t=0)}$ between the three heat treatment conditions tested is minimal. At the deepest indentation depths, $h_0 = 1000$ and 2000 nm, $\sigma_{ind(t=0)}$ is largest for the peak-aged condition and this is consistent with the data shown in Fig. 4.1.

The indentation depth dependence of σ_{th} is weaker than that of $\sigma_{ind(t=0)}$. Power-law functions of h_f fitted to the data in Fig. 4.6(b) indicate that, for a given indentation depth, σ_{th} is greatest in the peak-aged condition followed by the as-quenched and finally the over-aged conditions.
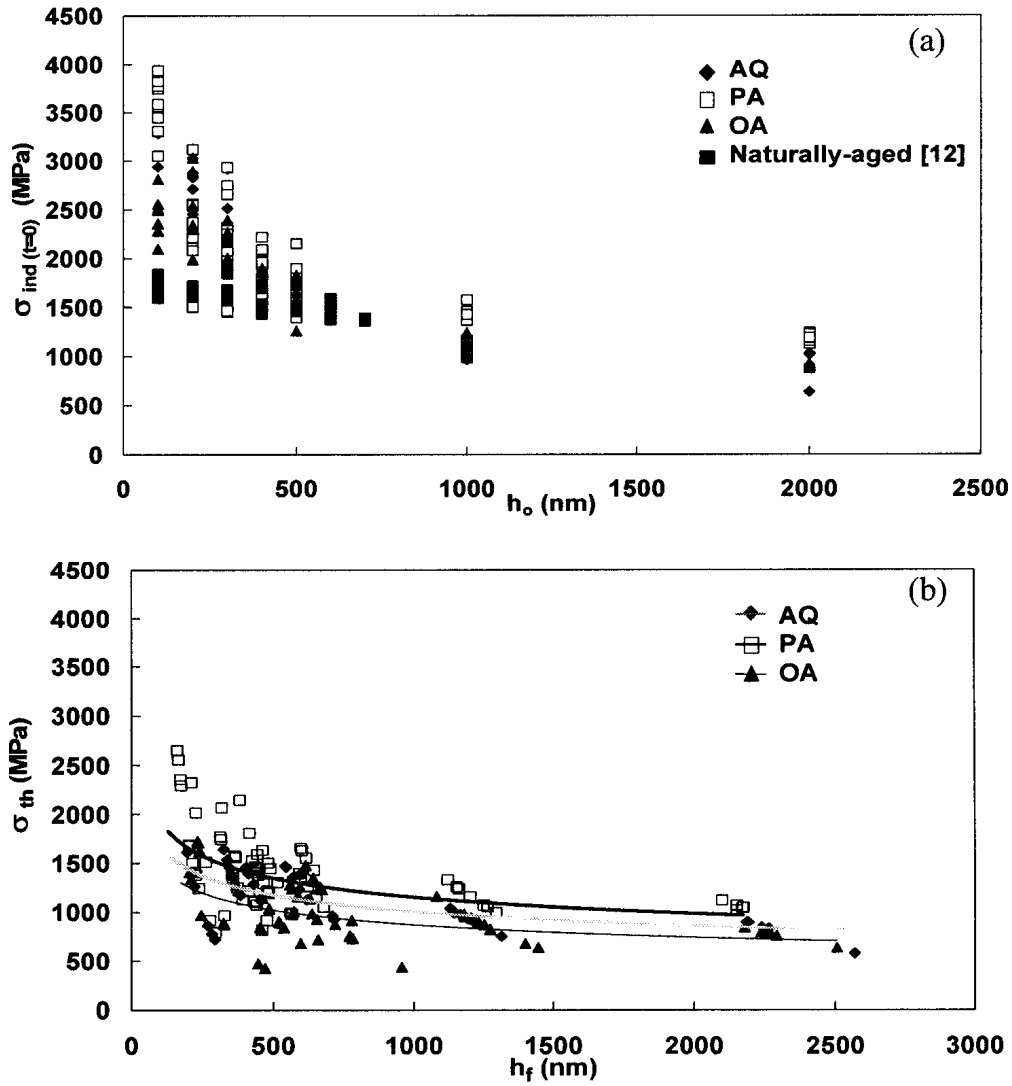
Figure 4.6: Variation in: **(a)** $\sigma_{ind(t=0)}$ with initial indentation depth, h_0 and **(b)** σ_{th} with final indentation depth, h_f for the 2024 aluminum alloy in the As-Quenched (AQ), Peak-Aged (PA) and Over-Aged (OA) conditions. $\sigma_{ind(t=0)}$ and σ_{th} both decrease with increasing indentation depth although $\sigma_{ind(t=0)}$ shows a stronger dependence upon indentation depth than does σ_{th}. The trend displayed by $\sigma_{ind(t=0)}$ is similar to that previously reported for the dependence of the indentation hardness of naturally aged 2024 aluminum alloy upon indentation depth [12]. The power-law functions fitted to the data in Fig. 4.6(b) indicate that σ_{th} is sensitive to heat treatment. σ_{th} is largest, for a given indentation depth, for the peak-aged condition followed by the as-quenched and finally the over-aged conditions.

4.4 Discussion

We now analyse the data from the indentation creep tests to assess the depth dependence of the parameters that describe the indentation creep rate; namely, $\Delta G(\tau_{eff})$, $\sigma_{ind(t=0)}$ and σ_{th}. We consider the effect of heat treatment on the depth dependence of these parameters. We then discuss the evolution of microstructure during constant-load indentation creep tests and relate the apparent activation volume of the deformation process to the combined effect of dislocation density and applied stress.

4.4.1 Dependence of $\Delta G(\tau_{eff})$ and ΔG_0 upon indentation depth and heat treatment

The apparent activation energy, $\Delta G(\tau_{eff})$ of the deformation process was calculated from the indentation creep data using Equations 4.1 and 4.2. Figure 4.7 shows $\Delta G(\tau_{eff})$, normalized with respect to the nominal strain energy of a dislocation of unit length, μb^2 (where μ_{al} = 25.4 GPa and b_{al} = 0.286 nm [13]), versus the effective average equivalent shear stress τ_{eff}. τ_{eff} was calculated as:

$$\tau_{eff} = \frac{\sigma_{ind} - \sigma_{th}}{3M\sqrt{3}} \tag{4.3}$$

Where M = 3.06 is the Taylor factor of aluminum [13]. The as-quenched, peak-aged and over-aged samples all show similar results: $\Delta G(\tau_{eff})$ increases with decreasing τ_{eff} but does not depend significantly upon the initial indentation depth nor does it depend upon the heat treatment condition.
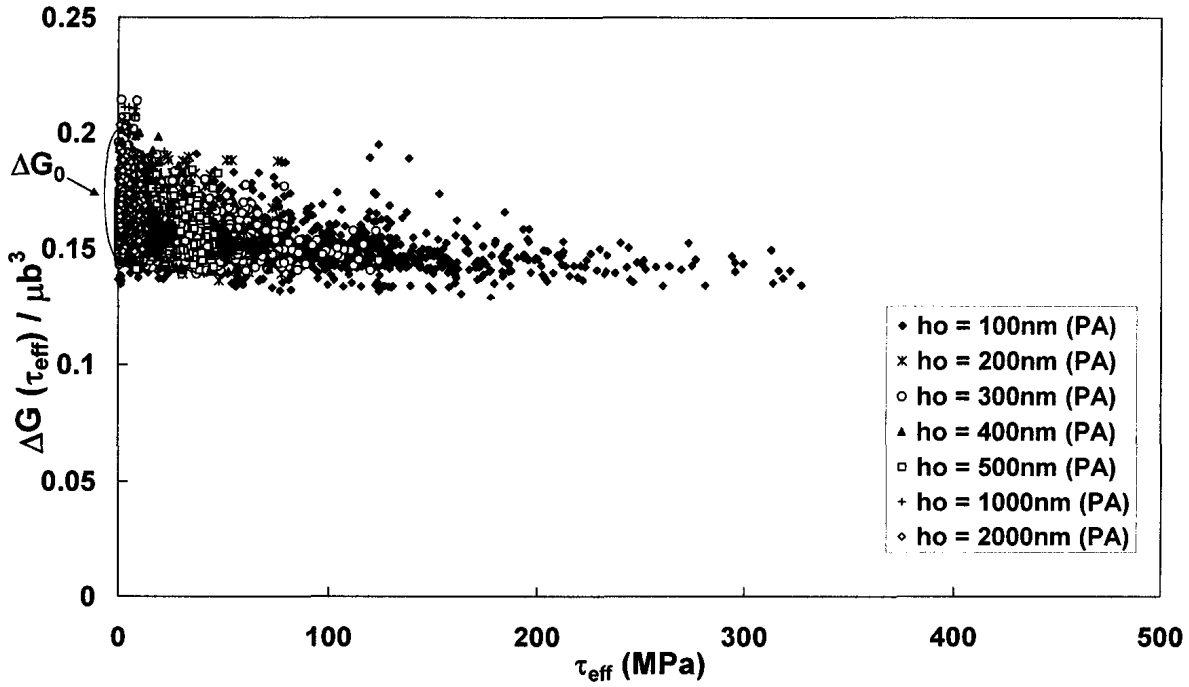
Figure 4.7: Thermal activation energy, $\Delta G(\tau_{eff})$, normalized with respect to μb^3, versus the effective indentation shear stress, τ_{eff}, for all indentation tests performed on the peak-aged 2024 aluminum alloy. Similar results were obtained for the over-aged and as-quenched conditions indicating that while $\Delta G(\tau_{eff})$ increases with decreasing τ_{eff} it is essentially independent of heat-treatment and indentation depth. Labelled on the plot is the apparent total activation energy ΔG_0 determined by extrapolating $\Delta G(\tau_{eff})$ to $\tau_{eff} = 0$.

The total apparent normalized activation energy, ΔG_0, of the deformation rate controlling obstacles was determined by extrapolating the $\Delta G(\tau_{eff})$ versus τ_{eff} trends to $\tau_{eff} = 0$ (Fig. 4.7). Figure 4.8 shows $\Delta G_0 / \mu b^3$ versus h_f for all the indentation depths from the three heat treatment conditions studied. For all cases ΔG_o ranges from 0.17 to 0.20 μb^3 and is not clearly different for any of the heat treatment conditions tested nor does it change significantly, beyond the scatter in the data, with indentation depth. Figure 4.8 shows, for comparison, previously published values of ΔG_o for pure polycrystalline gold at 300 K. ΔG_o for gold ranges from 0.11 to 0.17 μb^3 and is significantly lower than ΔG_o for the 2024 aluminum alloy. This suggests that the 2024 aluminum alloy has significantly

stronger obstacles to dislocation glide than those in pure metal such as gold. Our data show no consistent difference in the magnitude of ΔG_0 between the three heat treatment conditions for the 2024 alloy tested. Since all the samples tested in this study have the same chemical composition they may all contain second phase particles of very similar strength, ΔG_0, and these may be the primary obstacles limiting dislocation glide during indentation creep. The difference in the indentation creep rate between the different heat treatments conditions may then simply reflect the difference in the inter-particle spacing. This is discussed in the next section.
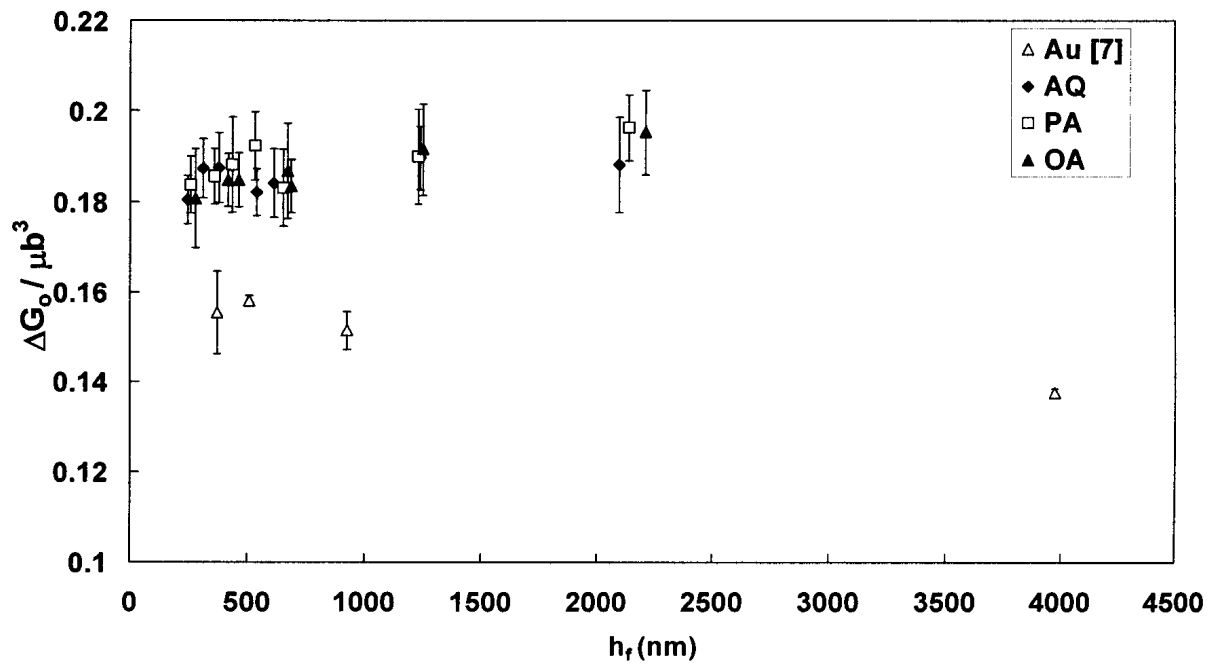
Figure 4.8: Average activation energy, $\Delta G_0/\mu b^3$ versus final indentation depth, h_f for As Quenched (AQ), Peak-Aged (PA) and Over-Aged (OA) samples of the 2024 aluminum alloy tested in this study and for polycrystalline gold [7]. The magnitude of ΔG_0 for the 2024 aluminum alloy ranges from 0.17 to 0.2 μb^3. ΔG_0 is larger for the 2024 aluminum alloy than for the gold indicating the effect of alloy additions on the activation energy of the deformation rate controlling obstacles.

4.4.2 Dependence of inter-obstacle spacing upon indentation depth and heat treatment

The parameters $\sigma_{ind(t=0)}$ and σ_{th} represent the flow stress of the tested material at the start and at the end of the constant-load creep test respectively. As such, both parameters are inversely related to the spacing of obstacle that limits dislocation glide. With that in mind, we consider the changes in $\sigma_{ind(t=0)}$ and σ_{th} shown by in Fig. 4.6 to result from changes in the average inter-obstacle spacing in the indentation plastic zone. This spacing can change with indentation depth, since the dislocation density around and indentation increases with increasing depth, or with heat treatment since second phase precipitates will interact and block dislocation glide.

The apparent average inter-obstacle spacing of the deformation rate controlling obstacles can be calculated by substituting either $\sigma_{ind(t=0)}$ or σ_{th} in place of σ_{ind} in the following equation

$$\ell^* = \mu b / \sigma_{ind} \qquad (4.4)$$

ℓ^* at the start of and at the end of the constant-load indentation creep tests is plotted versus indentation depth in Fig 4.9. At the start of the creep tests ℓ^* is dependent upon, and increases with, increasing depth (Fig. 4.9(a)). At the end of the creep tests ℓ^* is not strongly dependent upon indentation depth (Fig. 4.9(b)). This indicates that the average dislocation density around indentations, for all indentation depths, recovers during the one-hour constant-load creep tests and results in a recovered dislocation configuration that is relatively insensitive to indentation depth.
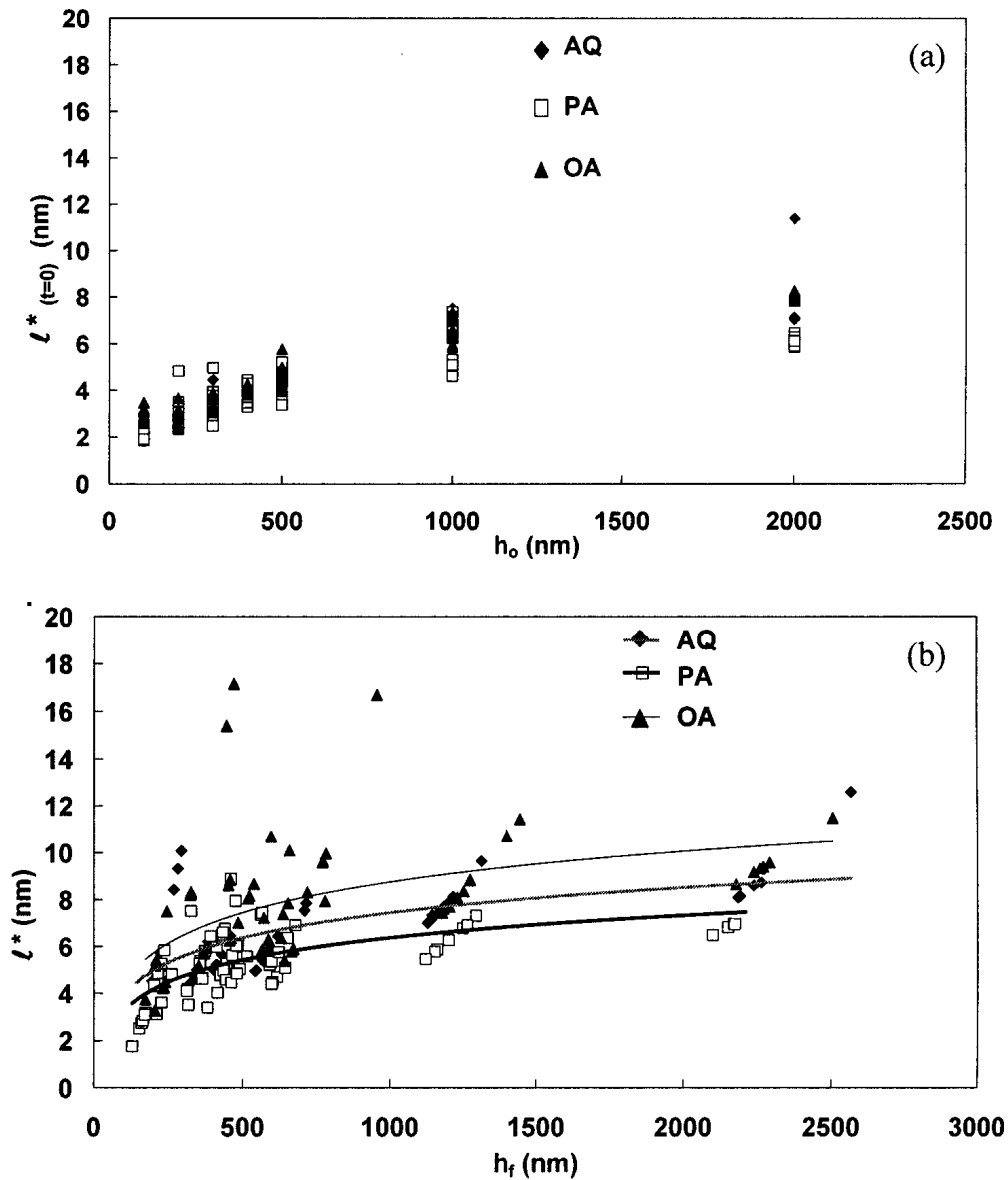
Figure 4.9: Nominal inter-obstacle spacing ℓ* (Eq. 4.4) for the 2024 aluminum alloy in the As-Quenched (AQ), Peak-Aged (PA), and Over-Aged conditions at: **(a)** the start of the indentation creep test versus h_0 and **(b)** the end of the indentation creep test versus h_f. ℓ* increase, in both graphs, with increasing indentation depth although ℓ* at the start (Fig. 4.9(a)) shows a clearer dependence upon indentation depth. The power-law functions fitted to the data in Fig 4.9(b) indicate that ℓ* is sensitive to heat treatment and is smallest, for a given indentation depth, for the peak-aged condition followed by the as-quenched and finally the over-aged conditions.

Fitting the data in Fig. 4.9(b) with power-law functions of indentation depth indicate that, on the whole, ℓ^* at the end of the one-hour creep tests is smaller, for a given indentation depth, for the peak-aged condition than for either the as-quenched or over-aged thermal conditions. More scatter is also present in the ℓ^* data from the over-aged condition than for the peak-aged or the as-quenched conditions. This is consistent with there being larger, more inhomogeneously spaced, second phase particles in the over-aged condition than in either the peak-aged or the as-quenched conditions. In the peak-aged condition, finely dispersed coherent or semi-coherent precipitates are present throughout the microstructure and this corresponds to the peak-aged condition showing the smallest ℓ^* in Fig 4.9(b). The as-quenched samples initially have Cu dissolved in a supersaturated solid solution but stress-assisted precipitation of copper aluminide particles around the indentations is likely to occur during the course of the indentation creep tests. This results in a relatively uniform distribution of closely spaced obstacles to dislocation glide within the indentation plastic zone and, hence, the calculated ℓ^* falls between the trends established by the peak-aged and the over-aged conditions.

4.4.3 Dependence of the apparent activation volume upon indentation depth and heat treatment

Neither the applied stress nor the microstructure around the indentation remains constant during constant-load pyramidal indentation creep tests. The deformation rate at any time during the creep test is therefore a function of both the instantaneous driving stress, τ_{eff}, and the instantaneous dislocation density, ρ. We can describe the deformation process in terms of the apparent activation volume V^* associated with the movement of a dislocations past the rate controlling obstacles, of strength ΔG_0, by the following energy balance

$$\Delta G_0 = \Delta G(\tau_{eff}) + \tau_{eff} V^* \qquad (4.5)$$

In this equation $\tau_{eff}V^*$ is the activation work that must be applied to overcome the obstacle. Constant-load indentation creep tests allow us to determine τ_{eff}, $\Delta G(\tau_{eff})$, and ΔG_0. We can therefore use Eq. 4.5 to calculate V^*. V^* changes as ρ and τ_{eff} change during the course of the creep test.
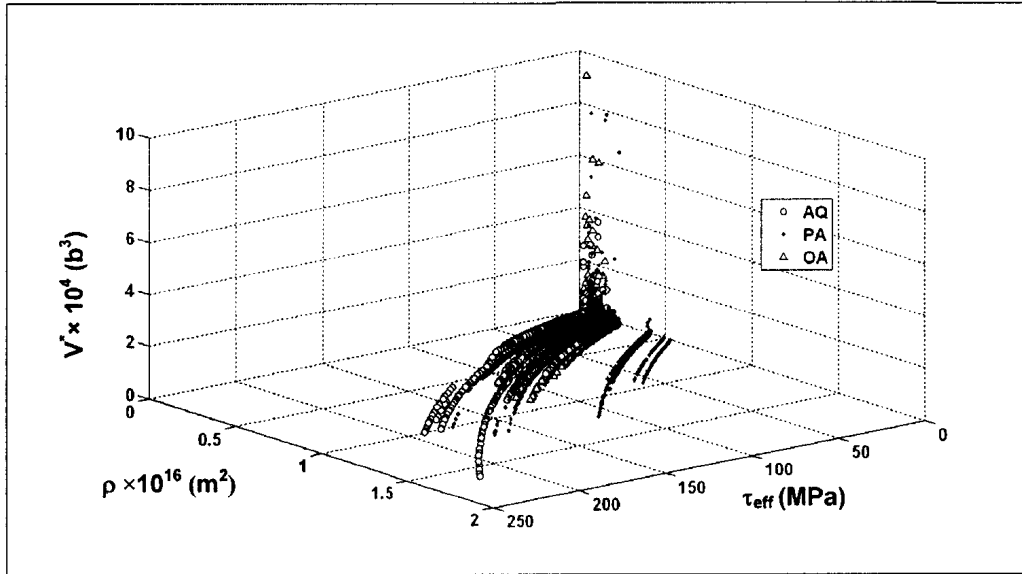
Figure 4.10: Apparent activation volume, V^*, versus nominal dislocation density, $\rho = [\sigma_{ind}/\mu b]^2$, and average effective indentation shear stress, τ_{eff}, for the 2024 aluminum alloy. The data from all initial indentation depths are included in this plot. The as-quenched, peak-aged, and over-aged data fall on essentially the same surface in V^*-ρ-τ_{eff} space. This indicates that similar evolution of dislocation/obstacle structure occurs around the indentations of all depths in the three thermal conditions tested.

Figure 4.10 shows V^* versus the nominal dislocation density $\rho = [\sigma_{ind}/\mu b]^2$ and τ_{eff} for the 2024 aluminum alloy in the as-quenched, peak-aged, and over-aged conditions. The data from the three thermal conditions fall on essentially a single surface in V*-ρ-τ_{eff} space. Fig 4.10 can be thought of as a map of the indentation creep process for the 2024 aluminum alloy at 300K. Indentation creep tests performed at different indentation

depths will be performed under different dislocation densities thus V^*, for a given τ_{eff}, will be different. Similarly, different heat treatments result in different inter-obstacle spacings and since dislocations are impeded by these obstacles, result in different dislocation densities for a given τ_{eff}. Our observation that V^* falls on the same V^*-ρ-τ_{eff} surface indicates that the same basic dislocation/obstacle mechanisms control the indentation creep rate for the 2024 aluminum alloy in the as-quenched, peak-aged, and over-aged conditions regardless of indentation depth.

4.5 Conclusions

The following conclusions can be drawn from this investigation of the effect of heat treatment on the depth dependence of the nanoindentation creep rate of the 2024 aluminum alloy at 300K.

The apparent inter-obstacle spacing ℓ^*, within the indentation plastic zone at the start of an indentation creep test is dependent upon the indentation depth, however, ℓ^* increases with time under constant load to a value that is essentially independent of indentation depth. ℓ^* measured at the end of the creep test is less for the peak-aged than for the as-quenched or the over-aged conditions.

The apparent activation energy $\Delta G_0/\mu b^3$ of the deformation rate limiting obstacles in the 2024 aluminum alloy is larger than $\Delta G_0/\mu b^3$ for a pure metal such as gold. This reflects the effect of the alloy additions, either in the form of solid solution point defects or precipitates, on the strength of the dislocation/obstacle interactions occurring during nanoindentation creep. $\Delta G_0/\mu b^3$ is, however, not dependent upon indentation depth. This is similar to what was previously reported for pure gold.

The apparent activation volume V^* of the indentation creep process changes with time during the constant-load indentation creep test however when plotted against instantaneous dislocation density ρ and effective indentation shear stress τ_{eff} the data

from all three thermal conditions fall upon essentially a single surface. This suggests that the evolution of the microstructure in the 2024 aluminum alloy during indentation creep at 300K is essentially the same regardless of thermal condition. The difference in the measured indentation creep rate for the three thermal conditions is then only a result of the different spacing of obstacles within the microstructure. For example, the spacing between precipitates is smallest in the peak-aged condition and, therefore, this heat treatment results in a material with decreased indentation creep rates for a given value of τ_{eff}.

These findings present new information on the time-dependent evolution of the dislocation structure around nanoindentations and, in particular, the role of second phase precipitates on the evolution of the dislocation structure during indentation creep.

References:

[1] Li W. B., Henshall J. L., Hooper R. M., Easterling K. E., *Acta metal. Mater.* v.39 (1991), p. 3099

[2] Sargent P. M., Ashby M. F., *Mater. Sci. Tech.*, v. 8 (1992), p. 594.

[3] Takagi H., Dao M., Fujiwara M., Otsuka M. *Philos. Mag.* v. 83 (2003), p. 3959

[4] Newson W. R., Diak B. J., Saimoto S., *Thin Films: Stresses and Mechanical Properties VI*, v. 436 (1997), p. 359, MRS Publications, Warrendale, PA, USA

[5] Bhakhri V., Klassen R. J., *J. Mater. Sci.*, v. 41 (2006), p. 2259

[6] Bhakhri V., Klassen R. J., *J. Mater. Sci.*, v. 41 (2006), p. 2249

[7] Bhakhri V., Klassen R. J., *Scripta Mater.*, v. 55 (2006), p. 395

[8] Klassen R. J., Diak B. J., Saimoto S., *Mater. Sci. Eng.*, A 387-389 (2004), p. 297

[9] Diak B. J., Saimoto S., *Mater. Sci. Eng.*, A 319-321 (2001), p. 909.

[10] Saimoto S., Diak B. J., Upadhyaya K. R., *Mater. Sci. Eng.*, A 234-236 (1997), p. 1015.

[11] Schuh C.A., Mason J.K., Lund A.C., *Nature Materials*, v. 4 (2005), p. 617.

[12] Ro Y. J., Begley M. R., Gangloff R.P., Agnew S. R., *Mat. Sci. Eng.*, A 435-436 (2006), p. 333

[13] Frost H. J., Ashby M. F., "*Deformation-Mechanism Maps*', p.21, Pergamon Press (1982), Oxford

Chapter 5

Effect of Crystal Orientation and Grain Boundaries on the Nanoindentation Creep of a 2024 Aluminum Alloy at 300K

5.1 Introduction

The dependence of the yield stress σ_y upon grain diameter d can be expressed for most polycrystalline metals by the well known Hall-Petch equation. The same dependence of σ_y upon $d^{-1/2}$ can be reached with simple models involving dislocation pile-ups at grain boundaries [1,2]. The role of grain boundaries as obstacles to dislocation glide in ductile metals is therefore quite well established. The effectiveness of grain boundaries at impeding low temperature time-dependent dislocation glide is, however, not well understood. In this investigation we perform nanoindentation creep tests and crystallographic orientation characterizations with Electron Back Scattered Diffraction (EBSD) to assess the effect of crystal orientation, proximity to grain boundaries and grain boundary misorientation on the parameters that govern the nanoindentation creep rate of a polycrystalline 2024 aluminum alloy at 300K.

The nanoindentation creep tests in this investigation are performed on an aluminum alloy at T = 300K ($\approx 0.3 T_{melt}$). At this lowtemperature, and considering the high level of stress around the indentation, nanoindentation creep is likely to occur by a mechanism of obstacle-limited dislocation glide [3]. Under these conditions, the shear strain rate can be expressed in terms of the effective applied shear stress $\tau_{eff} = \tau_{applied} - \tau_{th}$ as:

$$\dot{\gamma} = \dot{\gamma}_0 \exp\left(- \Delta G(\tau_{eff})/kT\right) \tag{5.1}$$

Where τ_{th} (or σ_{th}) is the stress below which no creep occurs, $\dot{\gamma}_0$ is a material constant (10^6 sec^{-1}[3]), k is the Boltzman constant, and $\Delta G(\tau_{eff})$ is the thermal energy required for

dislocations to overcome the deformation rate limiting obstacles. The total activation energy of these obstacles is $\Delta G_0 = \Delta G(\tau_{eff} = 0)$. Since grain boundaries represent obstacles to dislocation glide, they should affect the magnitude of ΔG_0 in the vicinity of the boundary.

Bhakhri and Klassen [4-6] and Bose and Klassen [7] have demonstrated that constant force micro- and nano-indentation creep tests can be used to measure local values of ΔG_0 with spatial resolution less than ± 1 μm. They found that, while ΔG_0 is consistently within the range expected for dislocation-obstacle type interactions for the ductile materials that they studied, the scatter in the measured ΔG_0 increases as the indentation depth decreases. The scatter may be due to:

1) The increased tendency for surface roughness to cause inaccurate measurement of indentation depth when the actual indentation depth is very small.

2) The increased effect of local crystallographic orientation on the nature of dislocation-dislocation interactions when the indentation depth is small.

3) The proximity of regions microstructural irregularity such as a grain boundaries or precipitates which are themselves as big as the sub-micron depth indentations.

In this study we focus on the latter two possible sources for the scatter and use indentation creep tests to investigate the dependence of factors governing the indentation creep rate upon crystal orientation, proximity of the indentation to grain boundaries, grain boundary angular misorientation.

5.2 Procedure

5.2.1 Sample Preparation

Four samples, each 12 mm thick and 25.4 mm in diameter, were cut from a rod of commercial purity 2024 aluminum alloy. The samples were solution treated at 810 K for

24 hours followed by water quenching and then annealing at 460 K for 360 hours. The annealed samples were cold-rolled to 1.5mm thickness and then annealed at 870K for 2, 3, 5 and 10 minutes to promote recrystallization and various amounts of grain growth. The average grain diameter of the samples increased from 10 to 100 μm with increasing annealing time at 870K.
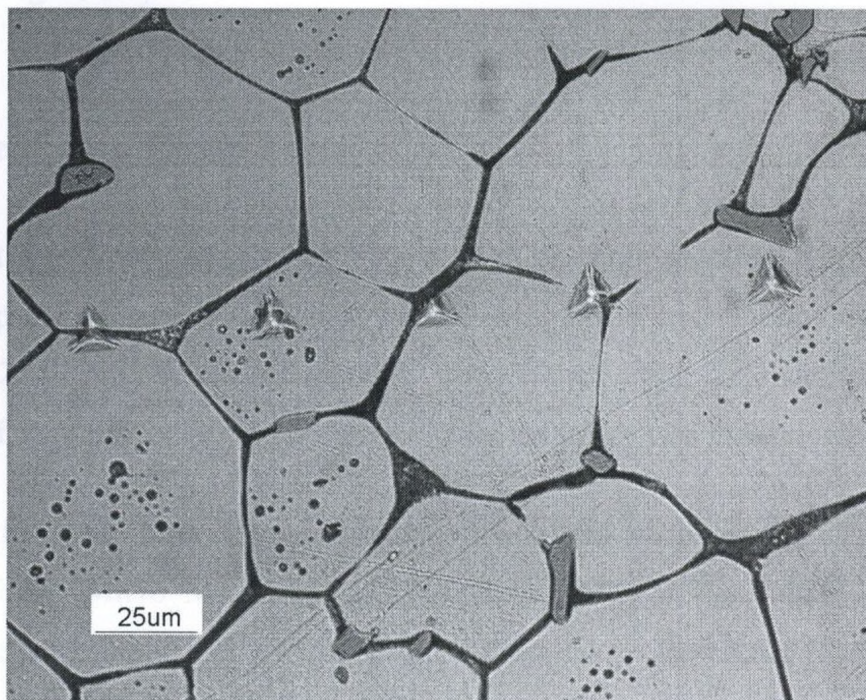
Figure 5.1:   Optical micrograph of an etched 2024 aluminum alloy sample. This sample was first electropolished and nanoindentation creep tests were performed on the electropolished surface. The sample was then electrolytically etched to reveal the grain boundaries. The figure illustrates the placement of some of the indentations in the interior of the grains while other indentations are placed directly on grain boundaries. Correlating the $\sigma_{ind(t=0)}$, σ_{th}, and ΔG_0, data from the individual indentation tests with the crystallographic orientation of the surface and the angular misorientation of nearest grain boundaries allows us to assess the effect of microstructural features on the local indentation creep rate.

The recrystallized samples were mechanically polished to a 0.05 μm surface finish and then electropolished in 7 vol% perchloric acid, 70 vol% ethanol, 20 vol% distilled water and 3 vol% butyl-cellosolve at 263 K at a current density of 1.5 A/cm^2 with a Stainless Steel Cathode. The average surface roughness of the samples after electropolishing was ± 5 – 7 nm. Indentation creep tests were performed on the electropolished samples. The samples were electrolytically etched after indentation testing to reveal the grain boundaries (Figure 5.1).

5.2.2 Indentation Creep Tests

Ten constant-force indentation creep tests, each of one hour duration, were performed on each electropolished sample at each of the following initial indentation depths; h_0 = 100, 500, 1000, 2000 nm. When the samples were etched after the indentation tests, the distance L of each indentation to its nearest grain boundary was measured.

The indentation creep tests were performed with a Micro Materials NanoTest indentation testing platform (Micro Materials Ltd., Wrexham, UK.) using a diamond Berkovich indenter. The performance of this instrument is described in Reference [8]. The first stage of each test was to increase the indentation force until the desired h_0 was reached. This was performed quite rapidly and h_0 was reached in about 15 seconds. The indentation load was then held constant for one hour during which time the indentation depth h was recorded at 18 second intervals. The indentation depth data were corrected for both thermal drift and elastic compliance of the indentation tester.

Figures 5.2 and 5.3 show plots of indentation force F versus h and h versus time for typical indentation creep tests performed at each level of h_0. The indentation depth increases continuously with time due to creep deformation.
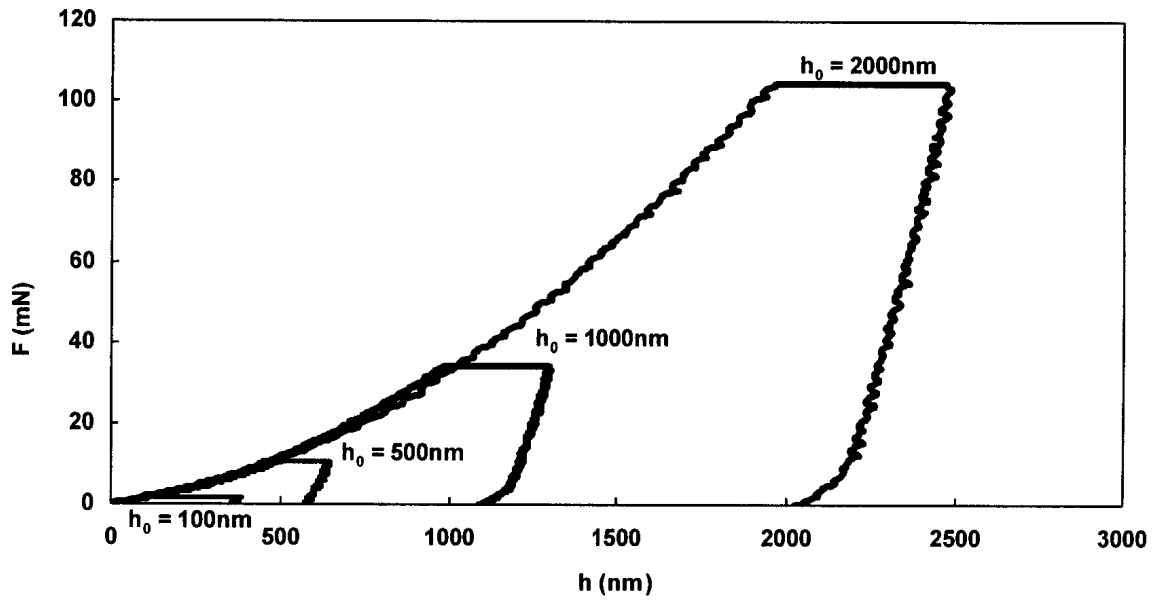
Figure 5.2: Indentation force F versus indentation depth h for indentation creep tests performed at h_0 = 100, 500, 1000, and 2000 nm. The flat regions of each curve represent the constant F stage of the test.
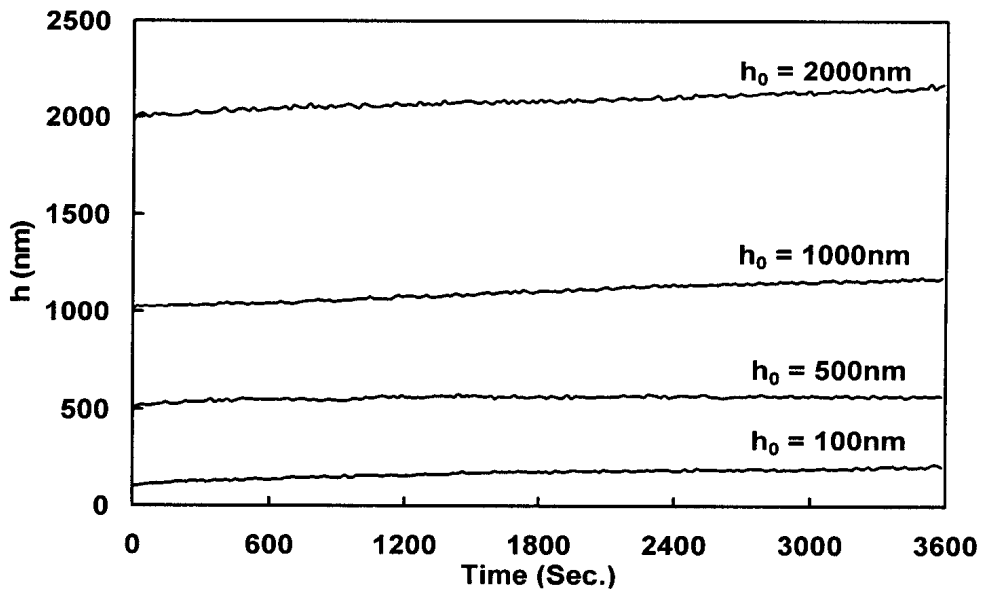
Figure 5.3: Indentation depth h versus time during the constant F stage of five indentation creep tests performed at h_0 = 100, 500, 1000, and 2000 nm. The h increases with time due to creep deformation and the average indentation stress and strain rate are calculated from these curves using Equation 5.2.

The average indentation stress σ_{ind} and the effective average indentation shear strain rate $\dot{\gamma}_{ind}$ were calculated as:

$$\sigma_{ind} = \frac{F}{24.5\alpha h^2}, \quad \dot{\gamma}_{ind} = \frac{\sqrt{3}}{h}\frac{dh}{dt} \tag{5.2}$$

where F is the indentation force and α is a geometric constant that accounts for the finite indenter tip radius. α was determined by measuring the projected indentation area from SEM micrographs of indentations, of various depths between 100 and 2000 nm, and comparing the measured area to that of an ideally sharp Berkovich indentation of the same depth. Previous research has shown that α is independent of h when indentations are performed with a Berkovich indenter [9].

5.2.3 Crystal Orientation Measurement

The test samples were electrolytically etched after the indentation creep tests and the average grain size and the minimum distance L from the edge of each indentation to its nearest grain boundary was measured using optical microscopy. Electron Back Scattered Diffraction (EBSD) analyses were performed around 18 indentations made on one of the samples. These indentations were of various values of h_0 and were located both within the interior of grains and near to, or directly upon, grain boundaries (Table 5.1). The EBSD measurements were made with a Nordiff EBSP camera unit attached to a Jeol 840 Scanning Electron Microscope operating at 20 keV. The Kikuchi diffraction bands emanating from the regions around the indentations were indexed to determine the hkl coordinates of the indented surface. For indentations made upon, or near to, grain boundaries, the angular misorientation θ of the boundary was calculated as the angle between the surface normal vectors of the two grains on either side of the boundary. For indentations made upon grain boundary triple points, the average angular misorientations across the three grain boundaries comprising the triple point was calculated and recorded.

Location of the indentation	Surface orientation	θ^* (degrees)	L (μm)	σ_{th} (MPa)	$\sigma_{ind(t=0)}$ (MPa)	$\Delta G_0/\mu b^3$
h_0 = 2000nm						
1. Interior of a grain	$(\bar{3}13)$	44.1	13.1	857	923	0.193
2. On a G.B.	$(\bar{1}25),(012)$	11.5	0	828	1153	0.193
3. On a G.B.	$(\bar{1}44),(\bar{2}13)$	33.1	0	841	916	0.189
4. Interior of a grain	$(\bar{1}21)$	39.5	15.4	816	910	0.184
5. Interior of a grain	$(\bar{1}48)$	39.5	13.8	715	844	0.190
h_0 = 1000nm						
6. Interior of a grain	$(\bar{1}56)$	39.5	13.3	932	1075	0.193
7. On a G.B.	$(\bar{1}09),(018)$	9.5	0	934	1201	0.190
8. Interior of a grain	$(0\ 1\ 12)$	34.8	11.1	974	1116	0.194
9. Interior of a grain	$(\bar{2}13)$	19.0	33.3	897	1092	0.191
10. On a T.J.	$(\bar{2}17),(\bar{2}13),$ $(\bar{1}14)$	14.7	0	988	1303	0.181
11. On a G.B.	$(\bar{1}01),(\bar{1}19)$	39.1	0	439	494	0.181
12. On a T.J.	$(\bar{6}17),$ $(012),(\bar{1}110)$	33.3	0	351	427	0.189
h_0 = 500nm						
13. Interior of a grain	$(\bar{2}12)$	Not avail.	28.3	1103	1360	0.182
14. On a G.B.	$(\bar{2}12),(013)$	42.5	0	973	1291	0.174
15. On a G.B.	$(013),(\bar{2}13)$	32.3	0	560	579	0.186
16. Interior of a grain	$(\bar{1}14)$	Not avail.	13	1283	1824	0.177
16. Interior of a grain	$(\bar{1}12)$	15.8	13	1017	2237	0.188
18. On a T.J.	$(\bar{1}56),(\bar{1}14),$ $(\bar{1}16)$	20.8	0	1300	1706	0.180

G.B. is Grain Boundary

T.J. is Triple Junction

*For indentations located within the interior of grains θ is the misorientation angle of the nearest grain boundary to the indentation. This grain boundary is located a distance L from the indentation.

Table 5.1: Data from the indentations made at different positions of the indexed grains on a 2024 aluminum alloy sample.

5.3 Results

Figure 5.4 shows σ_{ind} versus time during typical constant F indentation creep tests performed at various levels of h_0. σ_{ind} decreases with increasing time because h increases due to creep deformation while F remains constant (Equation 5.2). The rate of stress relaxation is very high in the early stages of the test and the shallow indentations display higher relaxation rates than the deeper indentations. After one hour the stress relaxation rate has decreased to the point where σ_{ind} becomes essentially constant. We therefore take σ_{ind} after one hour to be the apparent threshold indentation stress, σ_{th}, below which negligible further indentation creep occurs. The average initial indentation stress at the start of the constant F period of the test, $\sigma_{ind(t=0)}$, and σ_{th} are plotted versus h in Figure 5.5(a). $\sigma_{ind(t=0)}$, decreases with increasing h and this agrees with the previously reported depth dependence of the indentation hardness of naturally aged 2024 aluminum alloy [10]. σ_{th} shows a much weaker dependence upon h than does $\sigma_{ind(t=0)}$. This has also been reported previously and indicates that the recovered dislocation structure around a nanoindentation is much less dependent upon indentation depth than is the initial dislocation structure [4].
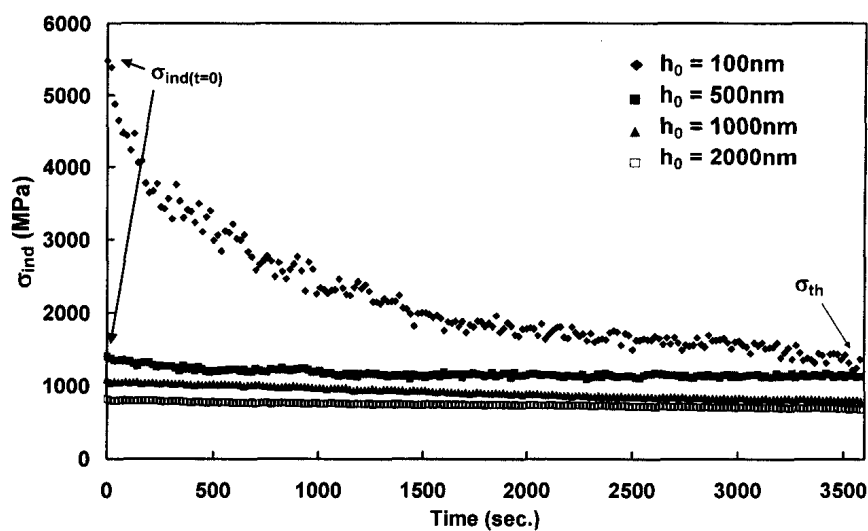
Figure 5.4: Average indentation stress σ_{ind} versus time during the constant F stage of indentation creep tests performed at h_0 = 100, 500, 1000, and 2000 nm. The initial indentation stress $\sigma_{ind(t=0)}$ and the threshold indentation stress σ_{th} are labeled on the plot.
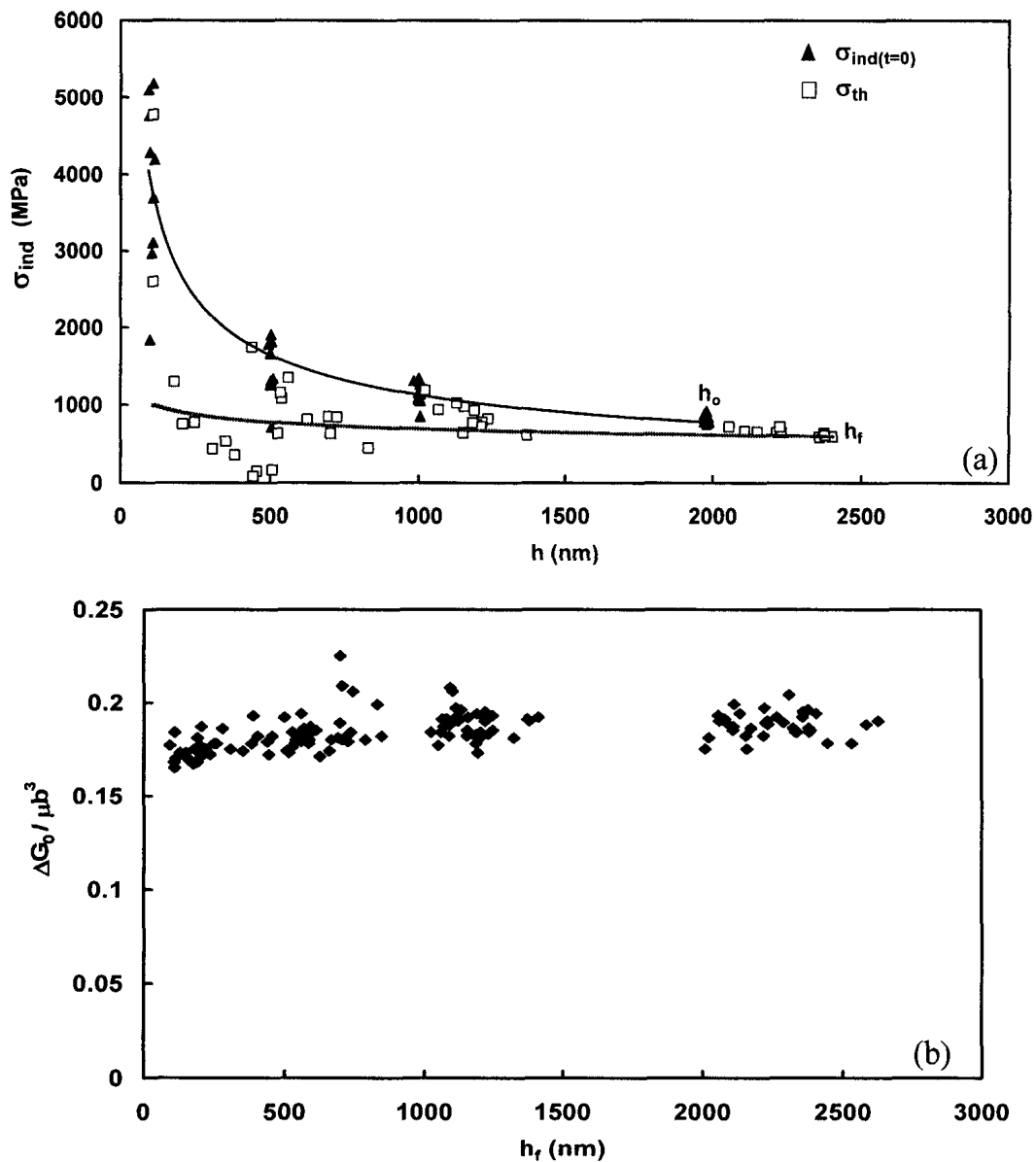
Figure 5.5: Dependence of (a) $\sigma_{ind(t=0)}$ upon initial indentation depth h_0, and σ_{th} upon final indentation depth h_f for one of the four 2024 aluminum alloy samples tested in this study and (b) $\Delta G_0/\mu b^3$ upon h_f for all samples studied. Both $\sigma_{ind(t=0)}$ and σ_{th} decrease with increasing indentation depth however $\sigma_{ind(t=0)}$ shows a higher rate of decrease than does σ_{th}. This suggests that the 'initial' dislocation structure around indentations is more sensitive to indentation depth than is the 'recovered' dislocation structure of the crept indentation [4]. $\Delta G_0/\mu b^3$ remains constant regardless of h_f. All the parameters show increased scatter when the indentation depth is small.

The equivalent effective average indentation shear stress τ_{eff} was calculated as

$$\tau_{eff} = \frac{\sigma_{ind} - \sigma_{th}}{3M\sqrt{3}}$$ (5.3)

where $M = 3.06$ is the average Taylor factor of aluminum [3]. Equation (5.2) was then used to calculate $\Delta G(\tau_{eff})$ for each test. $\Delta G(\tau_{eff})$ increases with decreasing τ_{eff} and this reflects the recovery with time of the dislocation structure in the region around the indentation [4-7]. The total apparent activation energy ΔG_0 was determined for each indentation creep test by estimating $\Delta G(\tau_{eff} = 0)$ by extrapolation of the $\Delta G(\tau_{eff})$ versus τ_{eff} curve to $\tau_{eff} = 0$. Figure 5.5(b) shows ΔG_0, normalized with respect to the energy of a dislocation of unit length μb^3 (where $\mu_{Al} = 25.4$ GPa and $b_{Al} = 0.286$ nm [3]), plotted against the indentation depth, h_f, at the end of the one hour creep test. ΔG_0 falls in the range from 0.17 to 0.20 μb^3 and does not display a clear dependence upon h_f however the scatter in ΔG_0 increases with decreasing h_f.

5.4 Discussion

The results presented in Figures (5.4, 5.5) indicate that the variability in $\sigma_{ind(t=0)}$, σ_{th}, and ΔG_0 increases with decreasing indentation depth. Possible sources for this scatter were listed in Section 5.1. The indentations presented in this study are relatively deep, ranging from $h_0 = 100$ to 2000 nm, in relation to surface roughness, $\pm 5 - 7$ nm. This suggests that the variability in the indentation data is not the result of surface roughness but rather the result of local variations in the microstructure of the sample. We therefore attempt to correlate $\sigma_{ind(t=0)}$, σ_{th}, and ΔG_0 to: 1) crystallographic orientation of the indented surface, 2) proximity of the indentation to a grain boundary and 3) the angular misorientation of the grain boundary. In this way we hope to find a connection with the variability in the measured parameters to the local microstructure at the region of the indentation.

5.4.1 Dependence of $\sigma_{ind(t=0)}$, σ_{th} , and ΔG_0 upon crystallographic orientation

Table 5.1 contains the data from nine indentations made in the interior of indexed grains. Figure 5.6 (a-c) show $\sigma_{ind(t=0)}$, σ_{th} , and ΔG_0 from these indentations plotted on a standard (111) stereographic triangle.

The data are grouped, in each plot, into two populations; shallow indentations (h_0 = 500 nm) and deep indentations (h_0 = 1000 – 2000 nm). The deep indentations have lower values of $\sigma_{ind(t=0)}$ and σ_{th} than do the shallow indentations. This agrees with the data trends shown, for a larger population, in Figure 5.5(a). In the case of $\sigma_{ind(t=0)}$, this reflects the commonly observed depth dependence of the initial dislocation structure around indentations [11-16].

Neither the $\sigma_{ind(t=0)}$ or the σ_{th} data show a clear dependence upon crystallographic orientation, the data from the shallow indentations show considerably more scatter than those from the deep indentations. This confirms the assessment of Lim and Chaudhri [17] who point out that the large number of easy-slip crystal planes in fcc metals necessitates that nanoindentation hardness should not depend upon the orientation of the indented surface.

The σ_{th}, in comparison to $\sigma_{ind(t=0)}$, is only slightly larger for the shallow indentations than for the deep indentations Figure 5.6(b) however the shallow indentations do show larger scatter in the data. As in the case for $\sigma_{ind(t=0)}$, the scatter in σ_{th} , appears to be random and not correlated to crystallographic orientation. The σ_{th} data from the deep indentations is much more uniform and clearly not dependent upon crystallographic orientation. The fact that σ_{th} is only slightly larger for the shallow indentations than for the deep indentations suggests that the dislocation structure around indentations that have been recovered through the process of creep are much less sensitive to indentation depth than

the "unrecovered" dislocation structure around a conventional nanoindentation. This has also been observed on nanoindentation tests performed on gold [3].
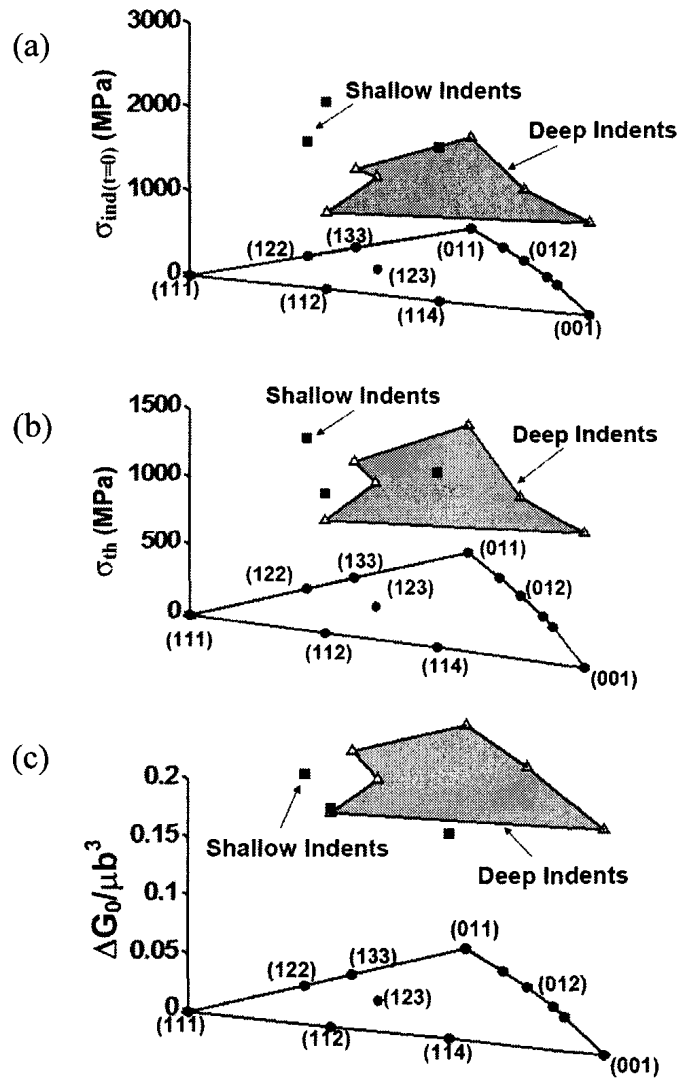
Figure 5.6: (a) $\sigma_{ind(t=0)}$, (b) σ_{th}, and (c) $\Delta G_0/\mu b^3$ from the constant F indentation creep tests performed on the interior of indexed grains (Table 5.1) plotted on standard (111) stereographic triangles. The data are grouped, in each plot, into two populations; shallow indentations ($h_0 = 500$ nm) and deep indentations ($h_0 = 1000 - 2000$ nm). The deep indentations have lower values of $\sigma_{ind(t=0)}$ and σ_{th} than do the shallow indentations. The $\Delta G_0/\mu b^3$ is not affected by indentation. Neither the $\sigma_{ind(t=0)}$, σ_{th} or $\Delta G_0/\mu b^3$ show a clear dependence upon crystallographic orientation however the data from the shallow indentations show considerably more scatter than those from the deep indentations.

The apparent activation energy ΔG_0 of the deformation rate limiting obstacles is not affected by either indentation depth or crystallographic orientation (Figure 5.6(c)). The ΔG_0 data all fall upon the same surface however the data from the shallow indentations show slightly more scatter than the data from the deep indentations.

5.4.2 Dependence of $\sigma_{ind(t=0)}$, σ_{th} , and ΔG_0 upon proximity to a grain boundary

In order to draw a correlation between the parameters $\sigma_{ind(t=0)}$, σ_{th} , and ΔG_0 with the distance L from the indentation to the nearest grain boundary we apply the following equation developed by Eshelby et al. [18] which gives the number N of dislocations in a dislocation pile-up of length L subjected to the equivalent indentation shear stress, τ_{ind}

$$N = \frac{L\tau_{ind}}{A} \tag{5.4}$$

We assume that the dislocation pile up consists of edge dislocations; thus, $A = \mu b/\pi(1-\upsilon)$. When the local shear stress τ_1 acting on the first dislocation nearest to the grain boundary exceeds a critical value, τ_{GB}, dislocations will begin to nucleate and glide through the grain on the other side of the boundary. This criterion is expressed as

$$\tau_1 = N\tau_{ind} = \tau_{GB} \tag{5.5}$$

Combining Equations (5.4 and 5.5) gives

$$\tau_{ind} = \left(\frac{A}{L}\tau_{GB}\right)^{1/2} \tag{5.6}$$

We assume that A and τ_{GB} remain constant; therefore, τ_{ind} , and therefore σ_{ind}, should be a linear function of $L^{-1/2}$. We recognize that the number of dislocations N_{ind} created during indentation must be sufficient to satisfy those required by Equation (5.4).

We can estimate N_{ind} by assuming that the indentation process induces dislocation nucleation at the indentation/sample interface with dislocation glide occurring along planes parallel to the sample surface with the dislocations piling up at the nearest grain boundary. N_{ind} can be estimated as the number of dislocations that are necessary to displace the indented material laterally to form the indentation. If we consider a slip plane parallel, and near to, the sample surface, N_{ind} can be expressed as

$$N_{ind} = \frac{h \tan \phi}{b} \qquad (5.7)$$

Where h is the indentation depth and ϕ is the included half angle of the Berkovich indenter tip ($\phi = 65.3°$).

Figures 5.7 (a-c) show $\sigma_{ind(t=0)}$, σ_{th}, and ΔG_0 plotted versus $L^{-1/2}$. The plots include data from the indentation creep tests where $N_{ind} > N$. The data from the $h_0 = 100$ nm tests and some of the data from the $h_0 = 500$ nm tests were therefore not included since for these tests N_{ind} is less than N. Neither $\sigma_{ind(t=0)}$, σ_{th}, or ΔG_0 show a dependence upon $L^{-1/2}$. This suggests that either these parameters are completely unaffected by the proximity of grain boundaries or that the use of Equations (5.4 and 5.6) to model the interaction of indentations with grain boundaries is a gross oversimplification. It must be remembered that these equations assume, that: 1) the grain boundaries are all normal to the sample surface, 2) the dislocations glide from the indentation to the grain boundary on planes that are parallel to the sample surface and 3) the boundaries all have the same strength τ_{GB}. These assumptions are clearly not correct and this could account for the scatter in the data. In the next section we present data to assess the effects of grain boundary orientation on $\sigma_{ind(t=0)}$, σ_{th}, and ΔG_0. This then allows us to reassess the dependence of these parameters on L by including into the expression terms describing the dependence of τ_{GB} on grain boundary orientation.
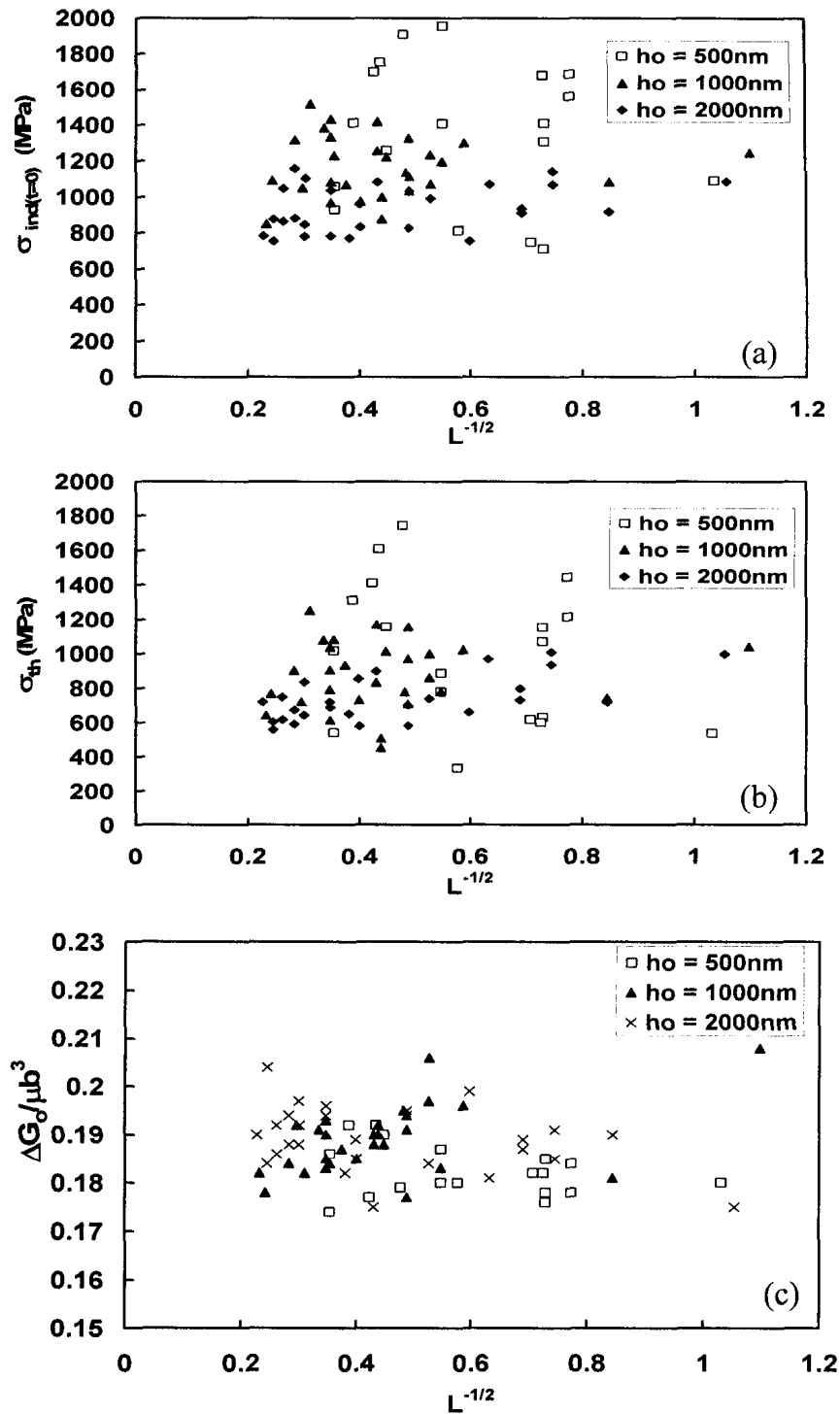
Figure 5.7: (a) $\sigma_{ind(t=0)}$, (b) σ_{th}, and (c) $\Delta G_0/\mu b^3$ versus $L^{-1/2}$. Neither $\sigma_{ind(t=0)}$, σ_{th}, or ΔG_0 show a dependence upon $L^{-1/2}$. The plots include data from all four 2024 aluminum alloy samples tested however the data from the $h_0 = 100$ nm tests and some of the data from the $h_0 = 500$ nm tests are not included since for these tests N_{ind} (Equation 5.7) is less than N (Equation 5.4).

5.4.3 Dependence of $\sigma_{ind(t=0)}$, σ_{th}, and ΔG_0 upon grain boundary misorientation

Table 5.1 contains $\sigma_{ind(t=0)}$, σ_{th}, and ΔG_0 data from 9 indentation creep tests performed directly upon grain boundaries and grain boundary triple junctions. We now compare these data with the angular misorientation θ of the boundaries.

Read and Shockley [19,20] proposed the following equation to describe the energy E, per unit area, of a small angle grain boundary in terms of θ

$$E = E_0\theta(B - \ln\theta) \tag{5.8}$$

In this equation E_0 and B are material constants. Equation 5.8 is derived by considering the grain boundary as an array of edge dislocations and is, therefore, only valid for small values of θ where the spacing between the dislocations comprising the grain boundary is large. Measured values of the relative grain boundary energies of tilt boundaries in iron and lead indicate that Equation 5.8 predicts the data well for boundaries of θ up to about 30 degrees [21-23]. Read [24] has also shown that Equation 5.8 is valid for general grain boundaries of random orientations.

Equation (5.8) indicates that E/θ is linearly related to $\ln\theta$. Since E is related to the effectiveness of a grain boundary as an obstacle to dislocation glide, the dependence of $\sigma_{ind(t=0)}/\theta$, σ_{th}/θ, and $\Delta G_0/\theta$ should also be linearly related to $\ln\theta$. Figure 5.8 (a,b) shows $\sigma_{ind(t=0)}/\theta$, σ_{th}/θ, and $\Delta G_0/\theta$ obtained from the 9 indentations made upon grain boundaries versus $\ln\theta$. The data show approximately linear trends. This suggests that $\sigma_{ind(t=0)}$, σ_{th}, and ΔG_0 in the regions very near to grain boundaries is related to θ in the functional form given in Equation 5.8.
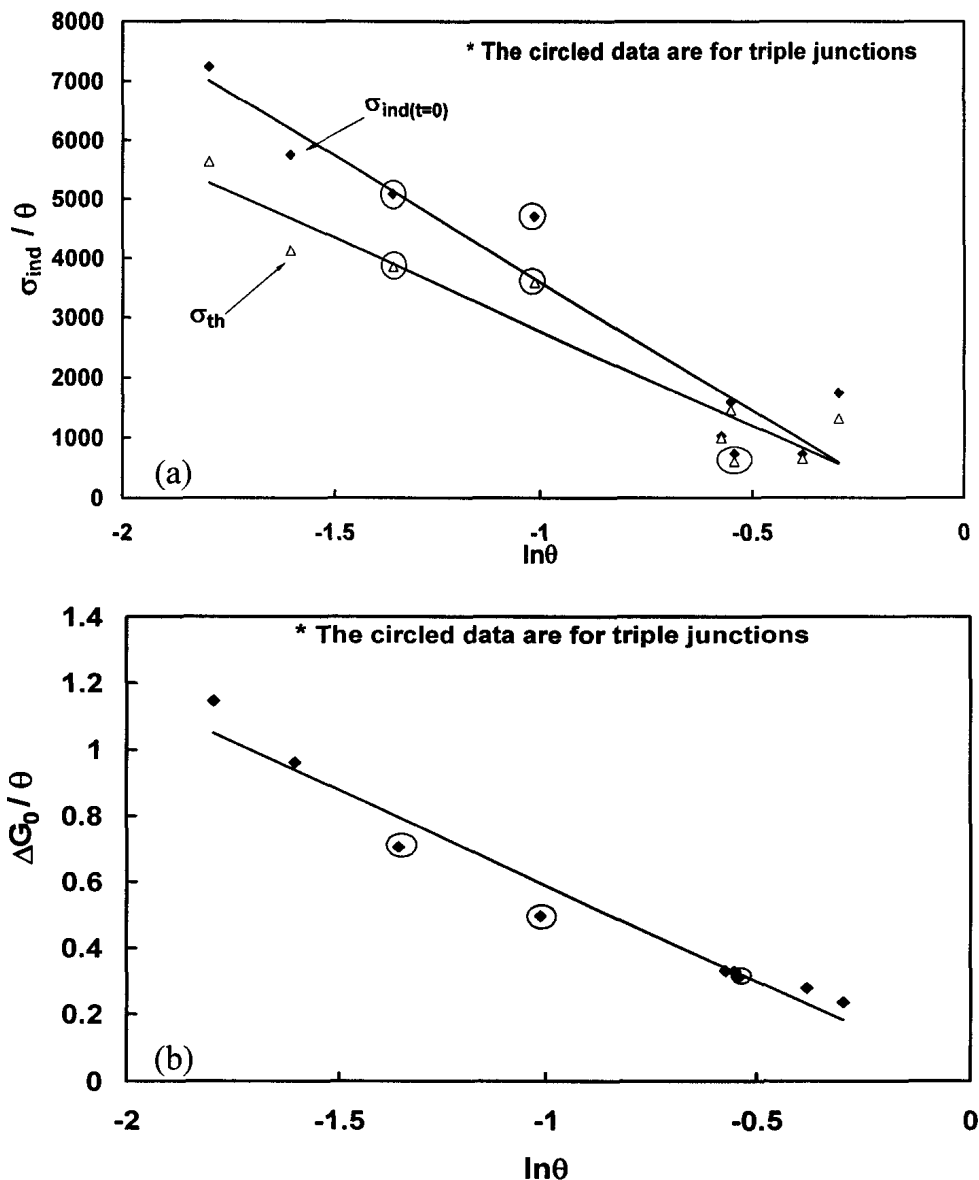
Figure 5.8: (a) $\sigma_{ind(t=0)}/\theta$, σ_{th}/θ , and (b) $\Delta G_0/\theta$ versus $\ln\theta$ from the constant F indentation creep tests performed on grain boundaries and grain boundary triple junctions (Table 5.1). The data in each figure show essentially linear relationships. This suggests that $\sigma_{ind(t=0)}$, σ_{th} , and $\Delta G_0/\mu b^3$ of grain boundaries are functionally related to θ in the same way as the Read Shockley equation (Equation 5.8).

Our observation that $\sigma_{ind(t=0)}$, σ_{th}, and ΔG_0 of grain boundaries is functionally related to θ can now be applied to revisit the dependence of $\sigma_{ind(t=0)}$, σ_{th}, and ΔG_0 , measured in the

vicinity of a grain boundary, upon the proximity L of the boundary. This is done by expressing the strength τ_{GB} of the grain boundary as a function of θ of the same form as Equation 5.8

$$\tau_{GB}(\theta) = C\theta(D - \ln\theta) \tag{5.9}$$

Where C and D are material constants. Substituting Equation 5.9 into Equation 5.5 gives the following expression for N

$$N = \frac{C\theta(D - \ln\theta)}{\tau_{ind}} \tag{5.10}$$

Substituting Equation 5.10 into Equation 5.4 results in the following expression for τ_{ind} as a function of θ and L

$$\tau_{ind}^2 = \left[\frac{AC\theta(D - \ln\theta)}{L}\right] \tag{5.11}$$

This equation indicates that $L\tau_{ind}^2/\theta$ will be linearly related to $\ln\theta$. Equation 5.11 gives the form of the functional relationship between parameters obtained from nanoindentation creep tests; namely, $\sigma_{ind(t=0)}$, σ_{th}, and ΔG_0 and L and θ of a grain boundary located near to the indentation.

Figure 5.9 (a-c) shows plots of $L\sigma_{ind(t=0)}^2/\theta$, $L\sigma_{th}^2/\theta$, and $L(\Delta G_0/\mu b^3)^2/\theta$ versus $\ln\theta$ for the nine indentation creep tests performed on the interior of indexed grains (Table 5.1). The trends in all plots are essentially linear confirming that Equation 5.11 captures quite well the actual dependence of the creep test parameters upon L and θ.

Figure 5.9: (a) $L\sigma^2_{ind(t=0)}/\theta$, (b) $L\sigma^2_{th}/\theta$, and (c) $L\left(\Delta G_0/\mu b^3\right)^2/\theta$ versus $\ln\theta$ for the nine indentation creep tests performed on the interior of indexed grains (Table 5.1). The trends in all plots are essentially linear confirming that Equation 5.11 captures quite well the actual dependence of the creep test parameters upon L and θ.
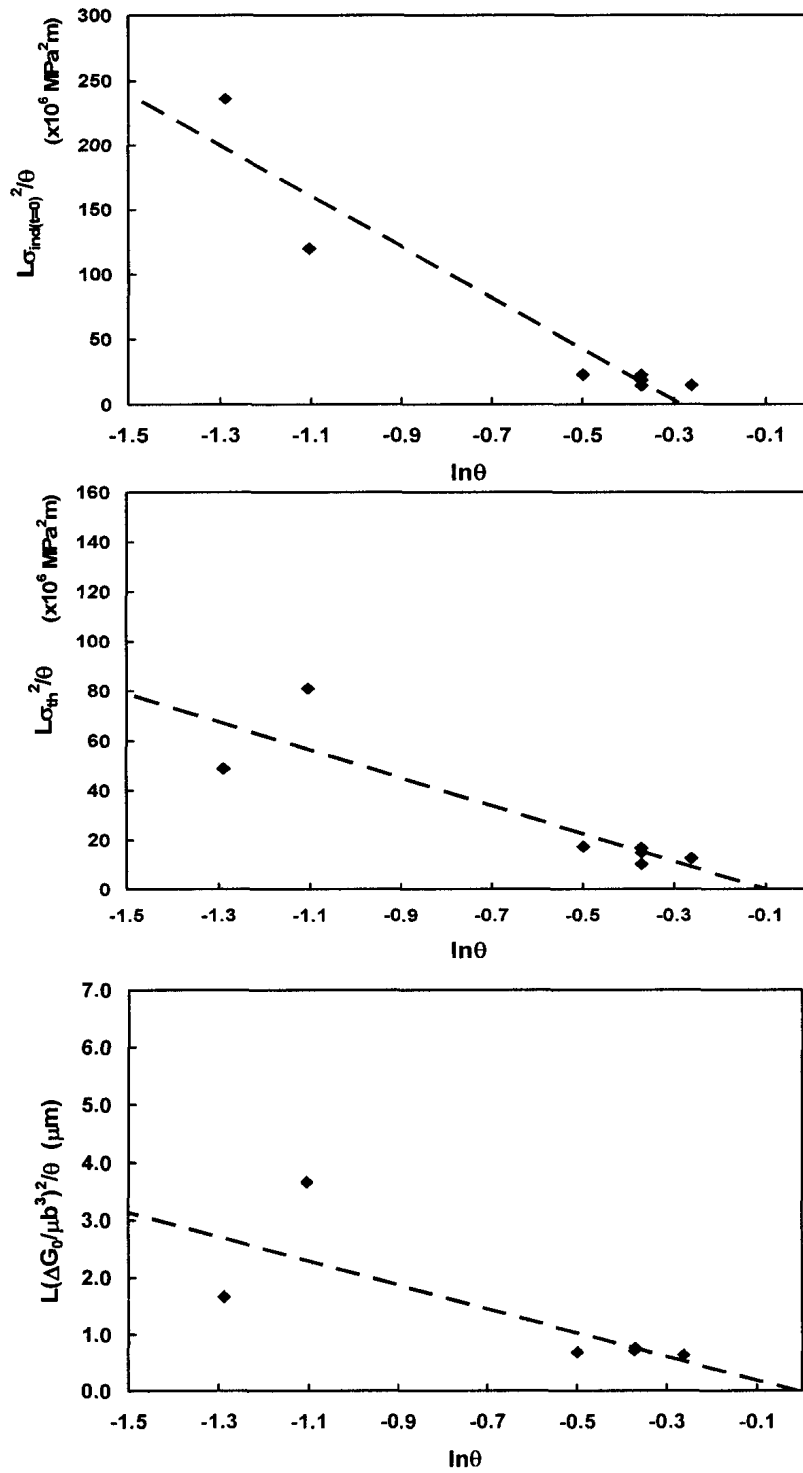
5.5 Conclusions

We have investigated the correlation of $\sigma_{ind(t=0)}$, σ_{th}, and ΔG_0, parameters that describe the constant F indentation creep rate in terms of the obstacle-limited dislocation glide, to crystallographic orientation of the indentation surface proximity of the indentations to grain boundaries and the angular misorientation of the grain boundaries.

By performing 160 constant F indentation creep tests at various indentation depths, between $h_0 = 100$ and 2000 nm, on the 2024 aluminum alloy at 300K we were able to demonstrate that the variability in the parameters $\sigma_{ind(t=0)}$, σ_{th}, and ΔG_0 increased with decreasing h_0 and the parameters themselves were not solely dependent upon $L^{-1/2}$.

We indexed the crystallographic orientation of a subset of the indented samples with and found no clear correlation between the magnitudes of $\sigma_{ind(t=0)}$, σ_{th}, and ΔG_0 with crystal orientation.

Indentation creep tests performed directly upon grain boundaries of known angular misorientation θ indicated that the measured $\sigma_{ind(t=0)}$, σ_{th}, and ΔG_0 of the boundaries could be expressed in terms of θ by equations of the same functional form as the Read-Shockley equation for the energy of a small angle grain boundary. This important finding demonstrated how nanoindentation creep tests can be used to directly measure mechanical properties of microstructural inhomogeneities such as grain boundaries.

The derived equations for $\sigma_{ind(t=0)}$, σ_{th}, and ΔG_0 as a function of θ were then applied to develop a modified Hall-Petch type equation that expresses $L\sigma_{ind(t=0)}^2/\theta$, $L\sigma_{th}^2/\theta$, and $L\left(\Delta G_0/\mu b^3\right)^2/\theta$ as linear functions of $\ln\theta$. These equations were shown to agree with our indentation creep data obtained from tests performed in the interior of indexed grains at a small distance L from a grain boundary of known angular misorientation.

The findings presented here suggest that much of the variability observed in nanoindentation test data, including data from constant F creep tests, arises from the inhomogeneous microstructure of the indented material. This then implies that nanoindentation testing can be used to assess quantitatively the properties of these microstructural features.

References:

1. N.J. Petch; *J. Iron Steel Inst.*, v. 174 (1953), p.25.

2. J.C.M. Li,Y.T. Chou; *Met. Trans.*, v.1 (1970), p. 1145.

3. H.J. Frost, M.F. Ashby, 'Deformation-Mechanism Maps', Pergamon Press (1982), Oxford, p. 21.

4. V. Bhakhri, R.J. Klassen; *Scripta Mater.* v. 55 (2006), p. 395.

5. V. Bhakhri, R.J.Klassen; *J. of Mat. Sci.* v. 41 (2006), p. 2249.

6. V. Bhakhri, R.J.Klassen; *J. of Mat. Sci.* v. 41 (2006), p. 2259.

7. B. Bose, R.J. Klassen; ; *J. of Mat. Sci* (in press).

8. B.D. Beake, J.F. Smith; *Philos. Mag.* A8 (2002), p. 2179.

9. K.W. McElhaney, J.J. Vlassak, W.D. Nix, *J. Mater. Res.* v. 13 (1998), p.1300.

10. Y. J. Ro, M. R. Begley, R.P. Gangloff, S. R. Agnew, *Mat. Sci. Eng.* A 435-436 (2006), p. 333.

11. N.A. Fleck, M.G. Muller, M.F. Ashby, J.W. Hutchinson, *Acta Metall. Mater.* v. 42 (1994), p. 475.

12. J.S. Stolken, A.G. Evans, *Acta Mater.* v. 46 (1998), p. 5109.

13. N.A. Stelmashenko, M.G. Walls, L.M. Brown, Y.V. Millman, *Acta Metall. Mater.* v. 41 (1993), p.2855.

14. M.S. De Guzman, G. Neubauer, P. Flinn, W.D. Nix, *J. Mater. Res. Symp. Proc.* v. 308 (1993), p. 613.

15. Q. Ma, D.R. Clark, *J. Mater. Res.* v. 10 (1995), p. 853.

16. W.J. Poole, M.F. Ashby, N.A. Fleck, *Scr. Metal. Mater.* v. 34 (1996), p. 559.

17. Lim Y.Y. and Chaudhri M. M., *Philosophical Magazine A*, v. 82 (2002), p. 2071

18. J.D. Eshelby, F.C. Frank, F.R.N. Nabarro, *Phil. Mag.*, v. 42 (1951), p. 351.

19. W.T. Read, W. Shockley, *Phys. Rev.*, v. 78 (1950), p. 275.

20. W.T. Read, W. Shockley, *"Imperfections in Nearly Perfect Crystals"*, Wiley, New York, (1952) Ch. 13.

21. C.G. Dunn, F. Lionetti, *Trans. AIME*, v. 185 (1949), p.125.

22. C.G. Dunn, F.W Daniels, M.J. Bolton, *Trans. AIME*, v. 188 (1950), p.1245.

23. K.T. Aust, B. Chalmers, *Proc. Roy. Soc. (London,)* A201 (1950), p. 210.

24. W.T. Read, '*Dislocations in Crystals*', McGraw-Hill (1953), p.173.

Chapter 6

Conclusions and Recommendations for Future Work

6.1   Conclusions

This thesis describes an investigation of the dependence of the indentation creep rate of polycrystalline 2024 aluminum alloy at 300K upon: 1) heat treatment, 2) indentation depth, 3) crystal orientation, 4) proximity to grain boundaries, and 5) grain boundary misorientation.   Constant load Berkovich indentation creep tests, of one hour duration, were performed at initial indentation depths of $h_0 = 100$ to 2000 nm.   The resulting average indentation strain rate was interpreted in terms of an obstacle-limited dislocation glide deformation mechanism (Equation 4.1).   The effect of the parameters mentioned above on: 1) the initial average indentation stress $\sigma_{ind(t=0)}$, 2) the final average indentation stress σ_{th}, and 3) the apparent activation energy ΔG_0 of the obstacles limiting the indentation strain rate was studied.

The effect of heat treatment and initial indentation depth was studied by testing samples in the as-quenched, peak aged and overaged condition. σ_{th} and $\sigma_{ind(t=0)}$ both decreased with increasing h_0. however $\sigma_{ind(t=0)}$ decreased at a faster rate than σ_{th}.. This indicates that the dislocation structure in the plastic zone around the initial indentation is highly sensitive to indentation depth, and this agrees with a bulk of previously published works, however, if the dislocations are allowed to creep for extended time, they recover into a structure that is much less dependent upon indentation depth.

The variation in $\sigma_{ind(t=0)}$ and σ_{th} with heat treatment reflects the expected dependence of inter-obstacle spacing upon heat treatment. In the 2024 series aluminum alloy, the strengthening comes from precipitates distributed throughout the microstructure. The spacing of the obstacles controlling the dislocation glide rate (as calculated from the

$\sigma_{ind(t=0)}$ and σ_{th} data) was smallest for the peak-aged condition which contains evenly distributed fine precipitates. Widely spaced larger second phase particles in the over-aged condition resulted in the largest value of inter obstacle spacing. The difference in the measured indentation creep rate is then only a result of the different spacing of the obstacles within the microstructure which depends upon both dislocation density (i.e.indentation depth) and heat treatment.

The apparent activation volume V* was calculated from the measured ΔG_0 (Equation 4.5) and was plotted versus instantaneous dislocation density ρ and effective indentation shear stress τ_{eff}. The data from all three heat treatments studied fall upon essentially a single V^*-ρ-τ_{eff} surface regardless of initial indentation depth. This indicates that the basic dislocation/obstacle interaction controlling the indentation creep rate of the 2024 aluminum alloy is independent of heat treatment and indentation depth.

The effect of grain boundaries and grain orientation on the deformation process during nanoindentation creep was also investigated in this thesis. Constant force nanoindentation creep tests were performed on polycrystalline 2024 aluminum at 300K to assess the dependence of $\sigma_{ind(t=0)}$, σ_{th} and ΔG_0 upon; 1) crystal orientation, 2) distance L to a grain boundary and 3) grain boundary misorientation angle θ.

$\sigma_{ind(t=0)}$, σ_{th}, and ΔG_0 did not depend upon the orientation of the indented surface and their dependence upon $L^{-1/2}$ did not follow a simple Hall-Petch form. Tests performed directly upon grain boundaries of known θ indicated that $\sigma_{ind(t=0)}$, σ_{th}, and ΔG_0 of the boundaries could be expressed in the same functional form as the Read Shockly equation for the energy of small angle boundaries (Equation 5.8). This demonstrates that nanoindentation creep tests can be used to directly measure mechanical properties of features such as grain boundaries. A modified Hall-Petch type equation was developed to express $\sigma_{ind(t=0)}$, σ_{th}, and ΔG_0 in terms of $(\theta(D - \ln\theta)/L)^{1/2}$ (Equation 5.11). The findings presented here suggest that much of the variability observed in the data from

nanoindentation tests arises from the inhomogeneous microstructure of the indented material.

6.2 Recommended Future Work

The findings of this research open several avenues for future research. Some of these are described below.

The finding that constant force nanoindentation creep tests performed directly upon grain boundaries can provide direct quantitative information on the strength and creep resistance of the boundary can be applied, in conjunction with EBSD measurements of local crystal misorientation, to study, and classify, a wide range of boundaries including interphase boundaries, boundaries containing nonequilibrium chemical segregation, high angle incoherent grain boundaries, and low energy Coincident Site Lattice (CSL) "special" boundaries. The possible types of internal interfaces that can be studied using this technique is virtually endless!

Alloy used in this investigation had an average grain size as low as $10\mu m$ however investigations, similar to those described in this thesis, could be carried out for ultra-fine grained or nano-crystalline materials to confirm the range of L and θ over which the derived Equation 5.11 is valid.

Transmission Electron Microscopy (TEM) can be used to observe the tiny precipitates present in the heat treated 2024 alloy and measure the exact amount of precipitates present in different heat-treatment conditions. This will then allow a more detailed assessment the influence upon the apparent activation volume V^* of interparticle spacing and dislocation density. In this study only a graphical representation of V^*-ρ-τ_{eff} was made however a more detailed assessment of these relationships would certainly be useful not only to further our level of knowledge of the fundamental deformation mechanisms but also to help in the development of optimal alloys and composites for highly specialized applications.